Heavy metal reinforcement in biomaterials: the influence of zinc on the mechanical properties of leafcutter ants mandibles

Auteur : Pavanetto, Lorenza
Promoteur(s) : Ruffoni, Davide; Compère, Philippe
Faculté : Faculté des Sciences appliquées
Diplôme : Cours supplémentaires destinés aux étudiants d'échange (Erasmus, ...)
Année académique : 2023-2024
URI/URL : http://hdl.handle.net/2268.2/20910

UNIVERSITÉ DE LIÈGE - UNIVERSITÀ DEGLI STUDI DI PADOVA
Faculté de Sciences Appliquées - Dipartimento di Ingegneria Industriale

Master thesis in Materials Engineering

Heavy metal reinforcement in biomaterials: the influence of zinc on the mechanical properties of the mandibles of the leafcutter ants *Acromyrmex octospinosus* workers

---

Promoters: Davide Ruffoni
Alessandro Martucci

Co-promoter: Philippe Compère

Co-supervisors: Albano Malerba
Astrid Cantamessa

Conducted by: Lorenza Pavanetto

ACADEMIC YEAR: 2023-2024

Abstract

The presence of zinc and other transition metals, such as bromine, manganese, and copper, is common in a variety of arthropods tools such as legs, claws, jaws and teeth. These elements provide an alternative form of reinforcement for biomaterials compared to the well studied biomineralization typical of mammalian bones. This type of reinforcement, in particular zinc, has been found in the mandibles of various species of leafcutter ants.
Leafcutter ants are fungus farming ants, meaning that they feed on a fungus cultivated in their nest on a substrate of fresh plant material. To sustain the fungus, they must cut fresh plant material daily. Consequently, their mandibles evolved to be very sharp and wear resistant to minimize the energy required for cutting an impressive amount of plant material throughout their lifetime.
In this work, various characterization techniques were used on the mandibles of *Acromyrmex octospinosus*, one of the known species of leafcutter ants, in particular two of the worker castes of this species were studied: "majors" and "minors", which have a different morphology and a different role in the ant colony.
Imaging techniques such as X-ray micro-computed tomography and digital microscopy were employed to acquire morphological information, scanning electron microscopy was used to obtain images of the mandible's internal part, and energy dispersive X-ray spectroscopy allowed us to acquire informations about zinc distribution in the mandibles. Different types of nanoindentation experiments such as quasi-static nanoindentation and wear resistance tests were performed both on *Acromyrmex octospinosus* and *Formica rufa* workers to characterize their mechanical properties. Stress-strain nanoindentation was used on the mandibles of an *Acromyrmex octospinosus* major worker to investigate its deformation behavior at the nanoscale.
Other studies have been conducted before on zinc-reinforced mandibles of different species of leafcutter ants, but this is the first one focusing on two different *Acromyrmex octospinosus* worker castes. The aim of this thesis is to make use of different characterization techniques, correlating them to expand knowledge on a biological material that is not extensively studied in the materials engineering field and that could inspire new engineered materials.
For both worker castes, indentation hardness and reduced elastic modulus of the zinc-reinforced areas of *Acromyrmex octospinosus* were found to be higher than in the non-reinforced areas. Wear tests, which have never been performed before on leafcutter ants, showed that the zinc-reinforced area of *Acromyrmex octospinosus* majors has an incredibly high wear resistance compared to the other tested areas of different samples. This work serves as a preliminary study on a relatively unexplored topic and aims to be a starting point for deeper and more extensive research.

Contents

1. Introduction

Over hundreds of millions of years of natural selection, animals have evolved tools with structures and chemical compositions finely tuned to allow them to perform specific functions, optimized for their environmental demands. In recent years, interest has grown in the study of these biological materials from an engineering perspective. This has led to the development of synthetic materials inspired by natural examples, such as spider silk, chameleon skin, and gecko foot hair. These biomimetic materials often offer enhanced functionality and sustainability, utilizing more environmentally friendly resources.

Some arthropod tools, such as spider fangs, scorpion stingers, and certain insect mandibles, have evolved to possess high hardness, stiffness, and wear resistance. These adaptations enable these structures to perform their functions with remarkable energy efficiency, making them a source of inspiration for the development of advanced synthetic materials. To successfully mimic these natural designs, it is essential to characterize their structure, composition, and properties of intere st.

The "tools" of many arthropods contain significant concentrations of unmineralized transition metals, strategically localized in areas requiring enhanced mechanical properties to function properly. Notable examples include copper in bloodworm *Glycera dibranchiata* tooth-like mouthparts [1], manganese in scorpion *Centuroides exilicauda* stings [2], zinc in marine polychaete *Nereis virens* jaws [3], spider's *Cupiennius salei* fangs [4] and finally in mandibles of leafcutter ants such as *Atta sexdens rubipilosa* [5].

In this work we analyzed two worker castes of *Acromyrmex octospinosus*, a species of leafcutter ant, with a focus on understanding the impact of zinc presence on the mechanical properties of their mandibles. The aim is to employ techniques commonly used in materials science and engineering to conduct a preliminary characterization of this interesting yet not widely explored material.

This thesis is structured into four main sections. The first section provides the necessary background information, beginning with an overview of the cuticle as a biomaterial and the various inorganic reinforcements in animal tools. It then offers a concise overview of *Acromyrmex octospinosus* society and the biological reasons for the specific mechanical properties of their mandibles. The introduction concludes with a theoretical explanation of the main characterization techniques used in the work.

The second section details the experimental procedures, including sample descriptions, instrumentation, and protocols followed during the experiments.

The third section presents results from various characterization techniques, including images and graphs obtained from X-ray micro-computed tomography (microCT), scanning electron microscopy (SEM), and nanoindentation tests.

In the final section, the findings are discussed in relation to existing literature, challenges encountered are addressed, and suggestions for future research are proposed.

1.1 Background

In this chapter, the cuticle is described as a biological material. Subsequently an overview of the different possibilities of inorganic enrichment for biological materials used for animals tools is provided. The background section concludes with a succinct discussion about the leafcutter ants society and labor division, necessary to understand the biological motivation behind the need fro high mechanical properties in their mandibles.

1.1.1 Cuticle

The cuticle is an extracellular layer that covers the entire external surface of insects and acts both as a skeleton for muscle attachment and as a protective barrier between the animal and its environment. It must provide a barrier to the environment and a shell that supports the body and a diverse set of tools in the form of functional appendages for locomotion, foraging, and defense, such as legs, wings, mandibles, and claws. All the different functions that cuticle has to perform make it a fascinating material due to its ability to adapt to the specific mechanical properties required for each function.

From a materials perspective, the arthropod cuticle is a hierarchical composite structure in which α-chitin crystallites, draped by proteins, form nanofibrils that organize into higher microstructural motifs.

The main component of arthropod cuticle is crystalline chitin, a water-insoluble polysaccharide composed of α-1,4-linked N-acetyl-d-glucosamine (GlcNAc) residues. Within the cuticle, the chitin crystallites in most arthropods are about 3 nm thick and at least 300 nm in length. Draped by chitin-binding proteins together they form the main structural unit of the cuticle: the nanofibrils. The protein-coated chitin nanofibrils consist of 18-25 chitin molecules arranged in antiparallel α conformation, resulting in a polygonal cross-section with a typical diameter of 2-5 nm and a length of about 300 nm. Within their assembly zone, an approximately 1.5 nm thick sheath of protein forms around the presumably self-organizing chitin fibrils. The chitin-protein nanofibrils are the smallest building blocks in the arthropod cuticle. In the majority of cases, the nanofibrils form the next level of structural hierarchy, the fibril planes. Where present, the chitin-protein fibers organize analogously to the fibrils and form planar arrays where the long axes of the fibers are parallel.

The lamellar appearance of the procuticle layers is formed by the stacking of fibril or fiber layers. A large number of configurations are possible, the most common and characteristic being the twisted plywood or Bouligand structure. This configuration is characterized by the fact that the long axes of the fibrils gradually rotate around the normal axis of the cuticle from one sheet to the next. More rarely, the fibril layers become stacked with the long axes of their fibrils in parallel, forming unidirectional arrangements. Such a cuticular architecture is mostly found in the endocuticle of structures that have to sustain unidirectional loading. The second-to-last level of structural organization is the bulk cuticle that forms the material of which the arthropod exoskeleton in its enormous variety of body plans consists.

Classically, the cuticle is subdivided into three main layers from the outside to the inside:

epicuticle, exocuticle, and endocuticle. The usually very thin epicuticle does not contribute significantly to the mechanical properties of the bulk cuticle, but it has many other vital functions for the animals. Twisted plywood and unidirectional lamellae can occur in both the exocuticle and endocuticle. Cuticle is usually horizontally layered, meaning the lamellae are oriented parallel to the cuticle surface, following the curvatures present in skeletal elements.

The versatility and adaptability of the cuticle's properties originate to a large extent from the variability in cuticular protein composition. Tens of different proteins may be found in each cuticle type. Some are structural, others are enzymatic, and some have both structural and enzymatic domains [6].

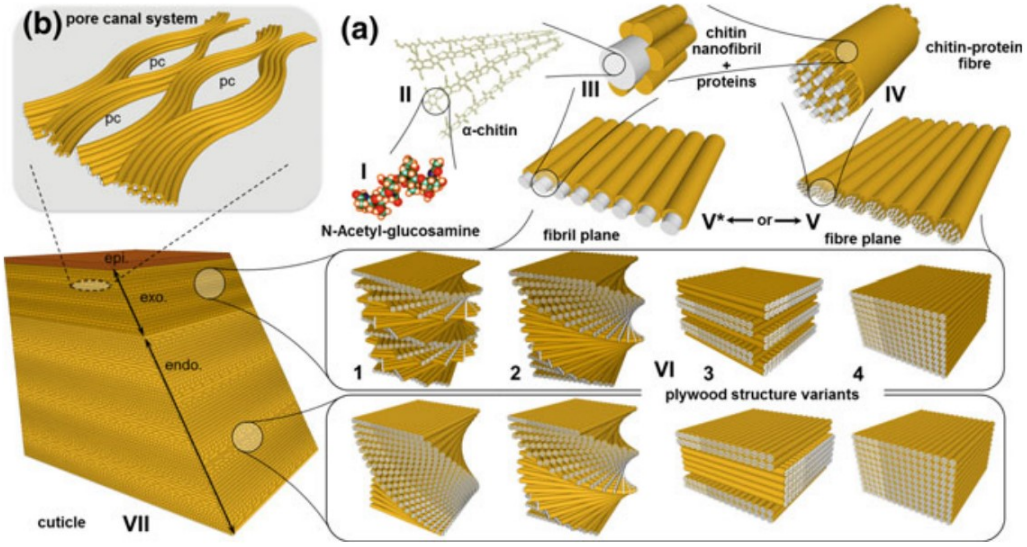

Figure 1: Schematic depiction of the structural organization of the organic phase in arthropod cuticle. N-Acetylglucosamine molecules (I) polymerize to form anti-parallel chains of α-chitin (II). Chitin crystallites coated with a protein layer form nanofibrils (III) that organize in parallel to form single fibril layers (V*). Alternatively, the nanofibrils can assemble to larger chitin-protein fibres (IV) that form horizontal fibre planes. (V). The fibril or fibre planes are horizontally stacked and form lamellae (VI) that can either be helicoidally stacked forming twisted plywood structures (VI 1, 2, 3) or unidirectionally stacked (VI, 4). Different variants of level (VI) constitute the procuticle layers. Together with the outermost epicuticle, the exo- and endocuticle form the basic material of the exoskeleton (VII). b The pore canal system is generated by deposition of fibrils/fibres around cellular protrusions during cuticle formation and it pervades the procuticle in normal direction. Figure from [6].

1.1.2 Inorganic reinforcement in animals tools

There are two distinct classes of inorganic-enriched biological materials used in claws, teeth, stings and other animal tools. The first class, biomineralized tissues, employ mainly Ca, Fe, and Si based minerals, like those in calcified teeth and bones or in the magnetite-filled teeth of certain mollusks. These biomineralized tissues contain two separate phases: an organic matrix and mineral inclusions that are usually larger than 100 nm in scale. The second class, "metal-

halogen" or "Heavy Element Biomaterials (HEBs), has heavy metals such as zinc, manganese, bromine, and copper, and halogens as dominant inorganic elements in concentrations between 1 and 25% of dry mass. While not as well understood as biomineralization, HEBs are at least as widely employed, occurring in many insect orders, in spiders and most other arachnids, in many centipedes, crustaceans, marine worms, and members of other phyla. HEBs are distinguished from biomineralized tissues by the apparent lack of separate organic and inorganic phases. Reinforcement in the mandibles of *Acromyrmex octospinosus* worker ants belongs to the second class; in particular, zinc is present in the region of the mandible close to the teeth lining. While biomineralized tissues are often filled with minerals to a degree that clearly alters the mechanical properties, it is not as obvious that the mechanical properties of HEBs are distinct from those of similar biomaterials that are not enriched, the investigation into mechanical properties of these types of materials is motivated by the location of the elements in the contact region of teeth, claws, jaws and stings. The advantage of heavy elements reinforcement over biomineralization has been hypothesized to be related to the ability to create sharper and more precise tools with smaller diameter tips. This feature is crucial, especially in small organisms, to perform specific tasks while minimizing the required energy [7]. The tiny, serrated "teeth" lining the inside edge of an ant's mandible is coated in a smooth blend of proteins crisscrossed with zinc. This material makes ants' teeth much better than the mammalian teeth for slicing and dicing, since the calcium phosphate crystals found in enamel can't form extremely sharp edges. Zinc, however, does not form blocky crystals; instead, it stays evenly distributed throughout the protein mixture, allowing for the sharp edges of the teeth.

1.1.3 Leafcutter ants ecology

Next to humans, leafcutter ants form one of the largest and most complex animal societies on Earth. All known species of leafcutter ants are endemic to South and Central America, Mexico, and parts of the southern United States. Leafcutter ants have a symbiotic relationship, called ant-fungus mutualism, with certain fungal species: they cultivate the fungus in their nest by providing freshly cut greens, protecting them from molds and pests, and clearing them of decaying material and garbage. The fungus in turn is a food source for the ants' larvae.

In the *Acromyrmex octospinosus* family, colony work is distributed based on caste and ant size as follows:

- The **"major"** workers are between 7 and 10 mm in size and are responsible of cutting and transport of plant material to the nest. They also transport eggs, larvae, and nymphs inside nest and take part in nest cleaning.
- The **"media"** workers are 4–7 mm in size and are responsible for nest building, expansion, and defense against external attacks. They also clean out waste, rejected plant material and dead ants.
- The **"minor"** workers are between 2 and 4 mm in size and are the most numerous. Their activity is primarily inside the nest, where they take care of the fungus. They inoculate mycelium through the plant material with their fecal fluid. They also take care for eggs, larvae and nymphs [8].

1.2 Characterization techniques

1.2.1 X-ray micro-computed tomography

X-ray micro-computed tomography, which will also be referred to as microCT, is a non-destructive radiographic imaging technique that allows to obtain three-dimensional images of an object's internal structure at a spatial resolution in the order of micrometers. An X-ray (radiography) system produces two-dimensional shadow images of complete internal three-dimensional structures, but in a single two-dimensional shadow projection, the depth information is completely mixed. Only an X-ray tomography system allows us to visualize and measure complete three-dimensional object structures without sample preparation or chemical fixation [9]. CT scans overcome the limitations of radiography by combining information from a sequence of 2D X-ray absorption images captured as the object rotates about a single axis, the data set after scanning consists of a series of normal transmission X-ray images. Using mathematical principles of tomography, this series of images is reconstructed to create a 3D digital image where each voxel (volume element or 3D pixel) represents the X-ray absorption at that specific point. Due to the relationship between X-ray absorption and material density, the 3D internal structure can be inferred from these images, and internal features can be accurately positioned. The resulting 3D images are typically visualized as a series of 2D slices [10].

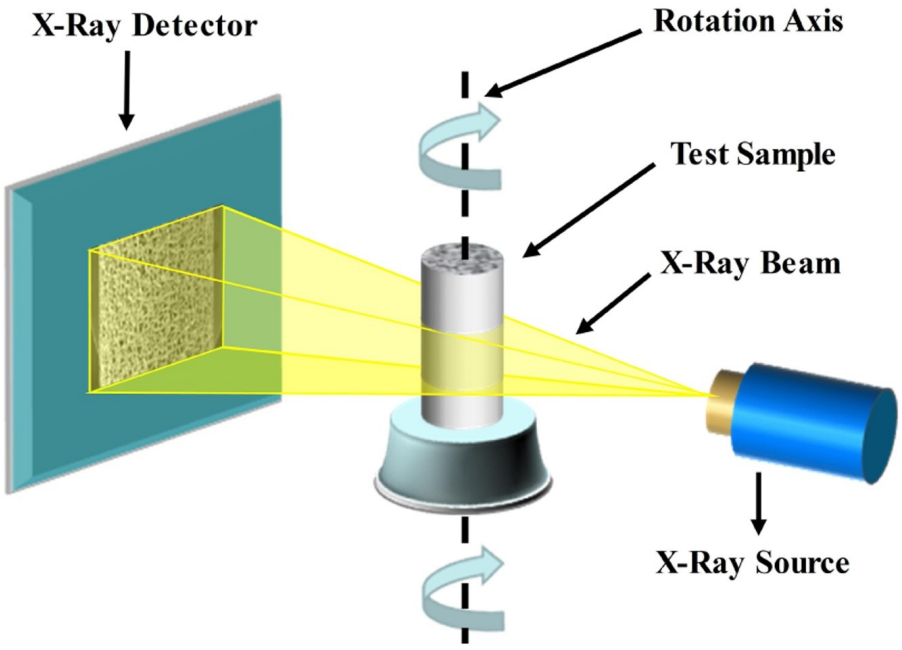

Figure 2: Schematic illustration of microCT system. Figure from [11].

1.2.2 Scanning Electron Microscopy

Scanning electron microscopy (SEM) is a technique that enables high-resolution analysis of material surfaces. The microscope operates based on the emission of primary electrons from an electron gun, that interact with the specimen. This interaction causes the ejection of atomic

electrons, and an image is formed by detecting the emitted electrons. Primary electrons are generated by either a thermal emission source or a field emission cathode and are accelerated to energies ranging from 1 to 40 keV, depending on the analytical requirements. Electromagnetic lenses within the SEM column focus these electrons into a narrow beam. Scanning coils located near the column's end direct and position this focused beam onto the sample surface.

Upon interaction with the sample, various signals are emitted due to the Coulomb field interaction between the incoming electrons and the specimen's nucleus and electrons. These signals include secondary electrons (SE), backscattered electrons (BSE), photons (X-rays used for elemental analysis), and visible light (these signals are shown Figure 3). Detectors collect these signals, which are then processed by a computer to generate the desired image. Different types of information about the sample can be observed depending on the detected signal.

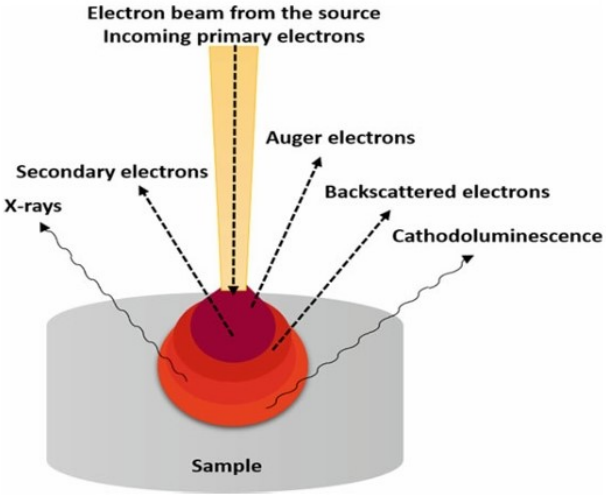

Figure 3: Signals emitted from a sample due to interaction with an electron beam. Figure from [12].

To create a SEM image, the incident electron beam is scanned in a raster pattern across the sample's surface. The emitted electrons are detected for each position in the scanned area by an electron detector. The intensity of the emitted electron signal is displayed as brightness on a cathode ray tube (CRT). By sychromizing the CRT scan to that of the scan of the incident electron beam, the CRT display represents the morphology of the sample surface area scanned by the beam [12].

The signals used for imaging are secondary electrons and backscattered electrons:

- **Backscattered electrons (BSE)** are electrons with energies comparable to the one of primary electrons. They are ejected by the elastic collision of an incident electron, typically with a sample atom's nucleus. The production efficiency for backscattered electrons is proportional to the material's mean atomic number, which results in image contrast as a function of composition, so higher atomic number materials appear brighter than low atomic number materials in a backscattered electron image, and this allows to obtain images with contrast as a function of elemental composition. One example of BSE image is reported in Figure 4a.

- **Secondary electrons (SE)** are lower energy electrons, typically with energies around 50 eV. They can be emitted either through collisions with the nucleus, where substantial energy loss occurs, or by the ejection of loosely bound electrons from the sample atoms. The topography of surface features affects the number of electrons that reach the secondary electron detector from any point on the scanned surface. This local variation in electron intensity produces the image contrast that reveals the surface morphology. An example of a SE image is shown in Figure 4b.

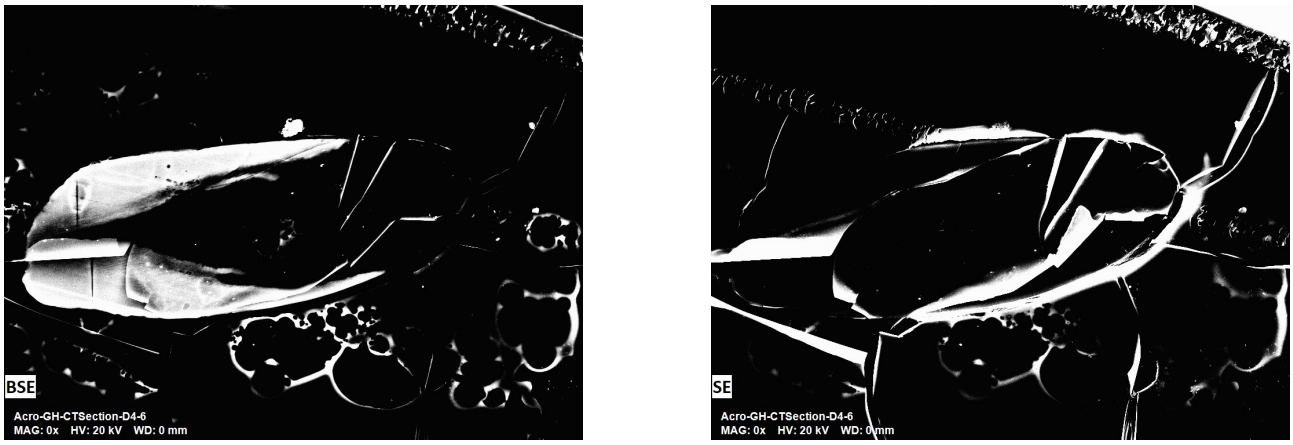

(a) **(b)**

Figure 4: Images of *Acromyrmex octospinosus* major worker mandible cut along transversal plane obtained with BSE 4a and SE 4b. In the BSE image the white area is the one containing zinc while in the SE image the surface morphology is more evident.

1.2.3 Energy Dispersive X-ray Spectroscopy

Energy dispersive X-ray spectroscopy (EDS or EDX) is a chemical microanalysis technique used in conjunction with scanning electron microscopy. It detects X-rays emitted from the sample during bombardment by an electron beam,enabling the characterization of the elemental composition of the analyzed volume. When the sample is bombarded by the SEM's electron beam, electrons are ejected from the atoms on the sample's surface, the resulting electron vacancies are subsequently filled by electrons from higher energy states, and an X-ray is emitted to balance the energy difference between the two electron states. The energy of the emitted X-ray is characteristic of the element from which it originated. The EDS X-ray detector measures the relative abundance of emitted X-rays as a function of their energy.

When an X-ray strikes the detector, it creates a charge pulse proportional to the energy of the X-ray. This charge pulse is converted to a voltage pulse by a charge-sensitive preamplifier, with the voltage remaining proportional to the X-ray energy. The signal is then sent to a multichannel analyzer, where the pulses are sorted by voltage. The energy of each X-ray, as determined from the voltage measurement, is sent to a computer for display and further data analysis. The spectrum of X-ray energy versus counts is analyzed to determine the elemental composition of the sampled volume. The spectrum shown in Figure 5a is relative to a specific

point of the sample. However, EDS can also provide elemental mapping of the entire surface by selecting elements of interest and generating images such as those in Figure 5b.

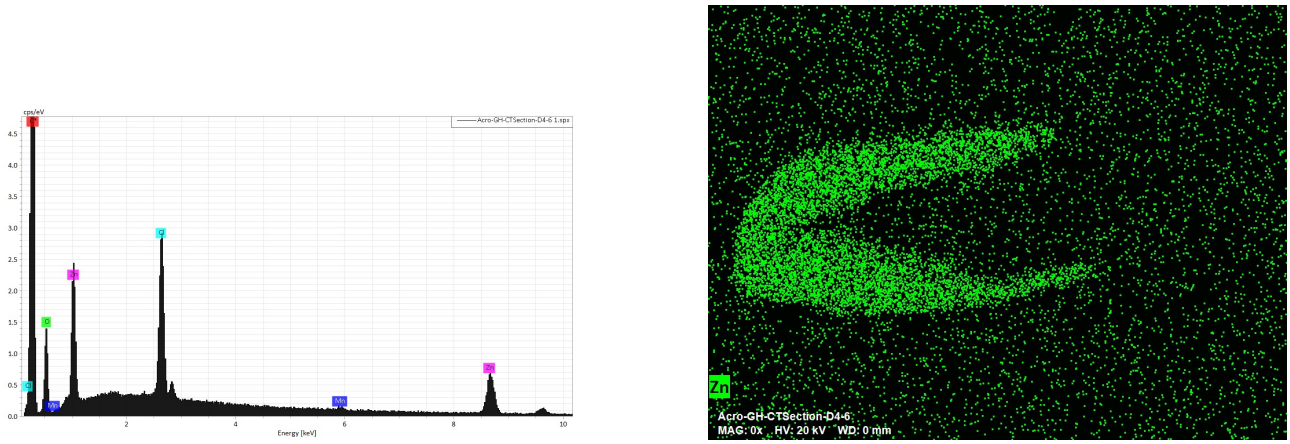

(a) **(b)**

Figure 5: Informations obtained with EDS about the elemental composition and distribution of zinc in a sample of *Acromyrmex octospinosus* major worker mandible cut along the transversal plane. In Figure 5a the X-ray spectrum of a specific point of the mandible is reported, illustrating the elements that are present in that point, with the heights of the peak indicating their quantity measured in cps/eV. Figure 5b shows the spatial distribution of zinc in the mandible.

1.2.4 Nanoindentation

Nanoindentation is a technique used to investigate the mechanical properties of materials at the nanoscale. Given the reduced dimensions of the subject of the specimen under study, nanoindentation is an essential technique for acquiring accurate mechanical information. In the following paragraphs the techniques that were used in this work are illustrated.

Quasi-static Nanoindentation

This indentation technique involves applying a defined load to a sample using a diamond tip with a precisely known geometry and measuring the resulting displacement. Different models can then be used to correlate the load-displacement data with the hardness and stiffness of the material.

The quantities shown in Figure 6b are:

- P_{max}: the peak indentation load
- h_{max}: the indenter displacement at peak load
- h_f: the final depth of the contact impression after unloading
- S: the initial unloading stiffnes

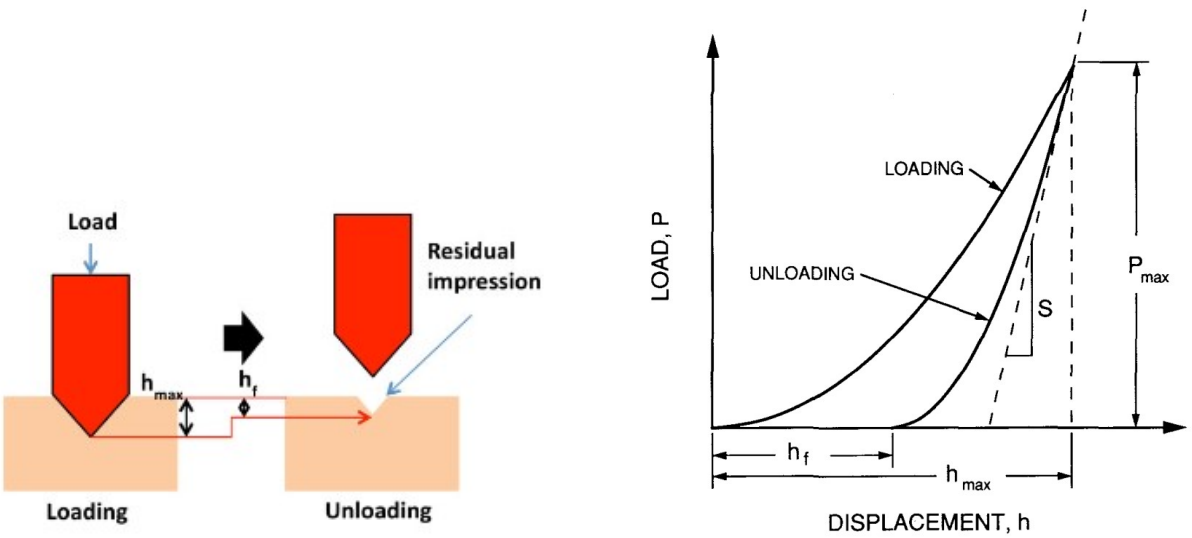

(a) **(b)**

Figure 6: Figure 6a shows the nanoindentation schematics while Figure 6b shows the loading and unloading curves in a and load versus indenter displacement graphs. Figures adapted from [13].

Quasi-static nanoindentation is used to obtain the reduced modulus E_r and hardness H of the material. In a standard quasi-static test, a controlled load is applied to a sample through a geometrically defined indentation probe. The probe depth is continuously measured so that the load-depth curve can be obtained. H and E_r can be extracted from this curve according to the Oliver-Pharr method [14] that will be shortly explain in the following paragraph.

H is obtained from Equation 1, where P_{max} is the peak indentation load and A is the projected area at the corresponding contact depth h_c.

$$H = \frac{P_{max}}{A} \tag{1}$$

E_r is a combination of the elastic modulus of the sample, i.e. E_S, and the one of the tip, i.e. E_t; it can be expressed as in Equation 2.

$$\frac{1}{E_r} = \frac{1-(\nu_s)^2}{E_s} + \frac{1-(\nu_t)^2}{E_t} \tag{2}$$

The reduced modulus is extrapolated as in Equation 4 from the fundamental equation of nanoindentation (Equation 3).

$$S = \frac{dP}{dh} = \frac{2}{\sqrt{\pi}} E_r A \tag{3}$$

$$E_r = \frac{\sqrt{\pi} S}{2\sqrt{A}} \tag{4}$$

Stress-Strain Nanoindentation

Stress-strain nanoindentation is a technique based on Hertz contact mechanics that differs from the classic quasi-static nanoindentation and allows to obtain the stress strain curves of a material at the nanoscale. The technique consists in loading the same nanoindentation site by applying a load function constituted by progressively increasing loads, as showed in Figure 7, and building the stress-strain curve at the nanoscale by associating load and displacement data to stress-strain data through Equations 5 and 6.

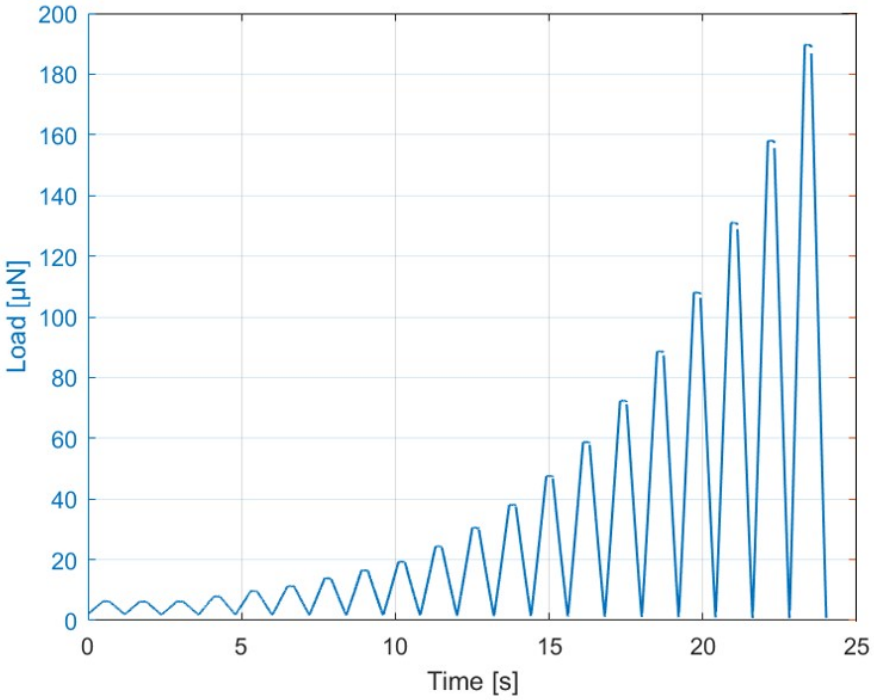

Figure 7: Load function applied to the selected location during our stress strain nanoindentation experiments.

$$\sigma = \frac{P}{\pi a^2} \tag{5}$$

$$\epsilon = \frac{a}{R} \tag{6}$$

P is the load, h_c is the contact depth and they are both obtained from the nanoindenter. a is the contact radius computed as illustrated in Equation 7 with C_0 and C_1 obtained during calibration in the standard material (fused quartz in our case). R is the tip radius calculated with Equation 8. The calibration technique is explained in the articles by Amini[15] and He[16]. The choice of the equation is based on the work of the master thesis by Sandront [17].

$$a = C_0(1 + h_c)^{C_1} \tag{7}$$

$$R = \frac{a^2}{2h_c} + \frac{h_c}{2} \tag{8}$$

Every indentation site is correlated to one stress-strain curve, and by plotting various of them in different indentation sites a more sophisticated analysis of the materials behavior under load and of the nature of deformation is possible. An example of a stress-strain curve obtained with this technique and plotted with the software Matlab R2024a is reported in Figure 8.

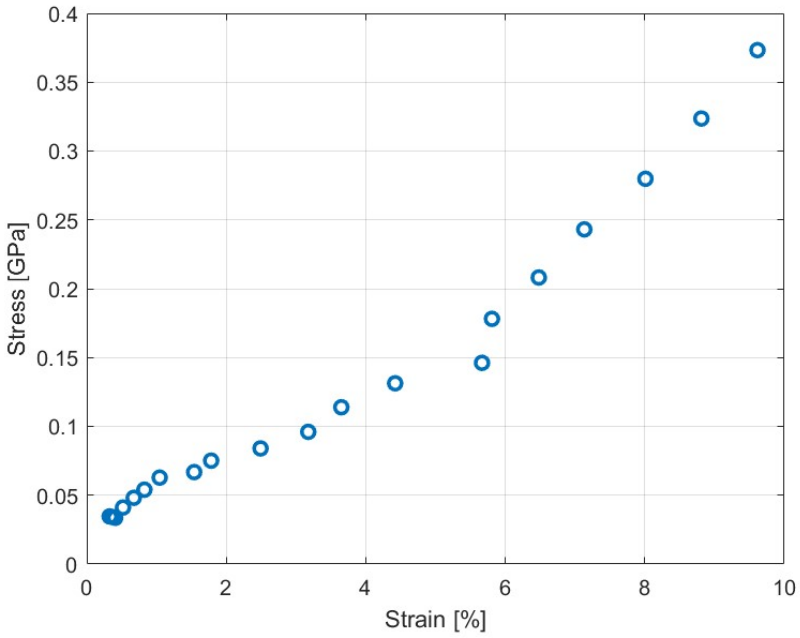

Figure 8: Stress strain curve at the nanoscale relative to one indentation location.

To measure the stress-strain response of the material, changing strain values are necessary during the course of the test, to meet this need a spherical tipped indent is a logical choice [16].

Wear test

Wear testing is another possible technique performed using the nanoindenter to evaluate the wear resistance of a material over a micrometric area. This technique is particularly relevant for the subject of this work, as wear resistance is a crucial property of leafcutter ant mandibles. The technique consists in using the Scanning Probe Microscopy (SPM) function of the nanoindenter (the technique is explained in Section 2.5.1) to scan the probe over a defined area of the sample multiple times, with an higher load compared to the one used to obtain surface topography. Before and after the test an SPM is performed on an area slightly larger than the tested one

to assess the topography and to observe the effect of the test on the sample. By comparing the topography of the tested area before and after the wear test some parameters to quantify wear resistance, such as the difference in the mean height of the tested area or the worn volume, can be ascerned.

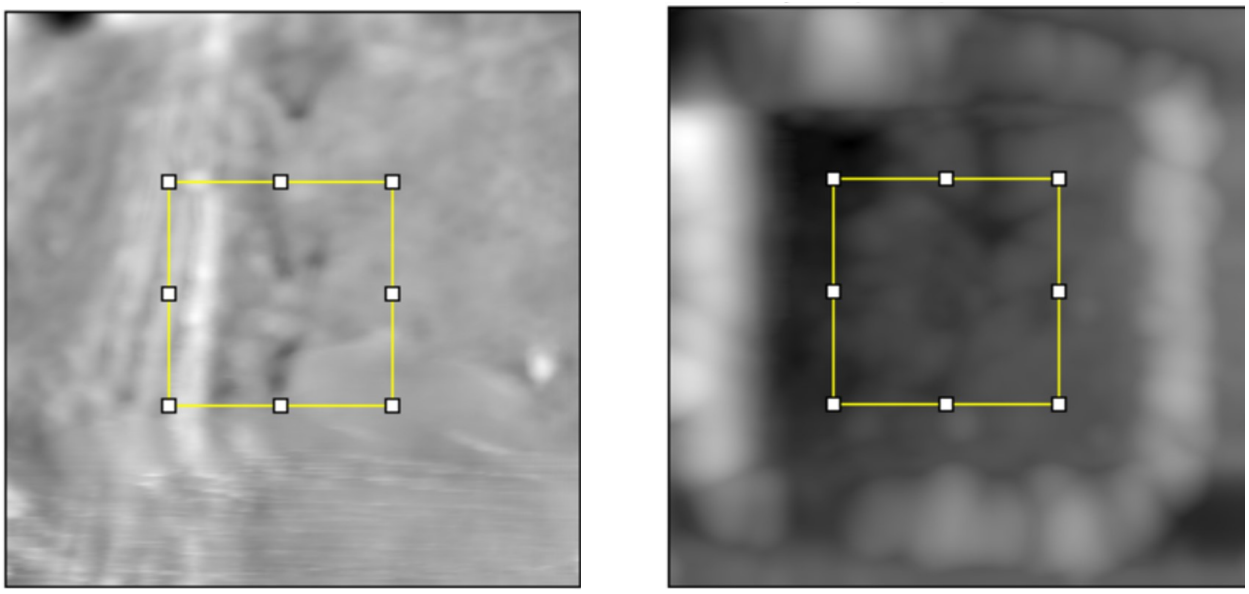

(a) **(b)**

Figure 9: SPM images processed with ImageJ of the same area before (9a and after (9b a wear test. The areas inside the yellow rectangles are the ones in which mean heights have been measured.

1.3 State of the art and aim of the thesis

A few studies explored mechanical characteristics of the mandibles of other species of leafcutter ants. In particular Johnston et al. used many different correlated characterization techniques to analyze the surface and subsurface layers within the zinc rich region of *Atta cepholotes* mandibles [18], while Schofield and colleagues measured hardness of the mandibular teeth of *Atta sexdens*, exploiting the fact that the zinc content in these ants mandibles increases with age to successfully correlate zinc content with hardness [5]. In both of these studies the ant species belong to the same tribe (Attini) but to a different genus (Atta).

Schofield et al. studied various mechanical properties of a serie of animal tools enriched with zinc and manganese. A multitude of tests were performed to obtain hardness, modulus of elasticity, impact resistance, energy of fracture and abrasion resistance of the materials in question[2].

Broomell et al. tried to establish a correlation between hardness and the presence of protein coordinated Zn^{2+} cations in Nereis jaws by chelating the metals with a specific treatment and comparing hardness before and after the cations removal [3].

Cribb and colleagues compared hardness and young modulus of six different termite species mandibles reinforced with zinc, manganese or not containing metals to investigate the comparative advantage of metal inclusion [19].

Another interesting study about metal reinforcement in animals tools has been conducted by Politi et al. on the spider fang, exploring its microstructure, chemical composition and relating mechanical properties with metal (zinc and calcium in this case) distribution [4].

Pontin et al. studied the *Glycera dibranchiata* toothlike mouthparts, which are enriched in different areas with unmineralized copper and atacamite fibers, with different characterization techniques [1], the wear resistance test conducted on the different microstructural domains that he found in this tool inspired us to perform the same test since wear resistance is a crucial property that was not tested on leafcutter ants yet.

The importance of wear resistance was demonstrated by Schofield and colleagues for *Atta cepholotes* by showing that ants with worn mandibles tend to carry leaves instead of cutting them [20].

In articles by Lichtnegger et al. [21] and Broomell at al. [3], a mechanism for zinc reinforcement in Nereis jaws was proposed, but the mechanism might not be the same for leafcutter ants since the quantity of zinc present in their mandibles is not the same, in fact the reinforcement mechanism in leafcutter ants has not been completely understood yet.

The aim of this thesis is to perform a multimodal characterization of the mandibles of *Acromyrmex octospinosus* worker ants, focusing on two different castes that have evolved to perform distinct tasks. This study examines their morphology, composition, and a range of mechanical properties.

Another goal is to investigate the relationship between the presence of zinc in certain areas of the mandibles, particularly those corresponding to the teeth lining, and the resulting increases in hardness, stiffness, and wear resistance. The research will look at differences in morphology, composition, and mechanical properties across different samples, and it will compare the mechanical properties of zinc-reinforced areas with non-reinforced areas within the same mandibles.

The techniques used in this work are being applied to this species of ants for the first time, and the results may be helpful for future research in this area or inspire the development of new bioinspired materials.

2. Materials and methods

2.1 Samples preparation

Acromyrmex octospinosus ants were collected in Guadalupe in February 2023 and preserved in absolute ethanol (Figure 10a) until March 2024, when the experimental part of this work began. Two different worker castes were collected: majors and minors. The heads of the major workers are four times larger than those of the minor workers (Figure 11).

The best samples were selected, and the ants were sectioned under an optical microscope using tweezers and a knife to separate the heads from the bodies. Some mandibles of the major workers were detached from the heads using the knife. This procedure was performed on a Petri dish containing a small amount of the absolute ethanol in which the ants were preserved, to prevent them from drying out.

To enhance resin penetration into the mandibles, which is important for adhesion between the resin and the biological sample, the backs of some heads were punctured with an awl. The samples were kept separate in Eppendorf tubes filled with absolute ethanol.

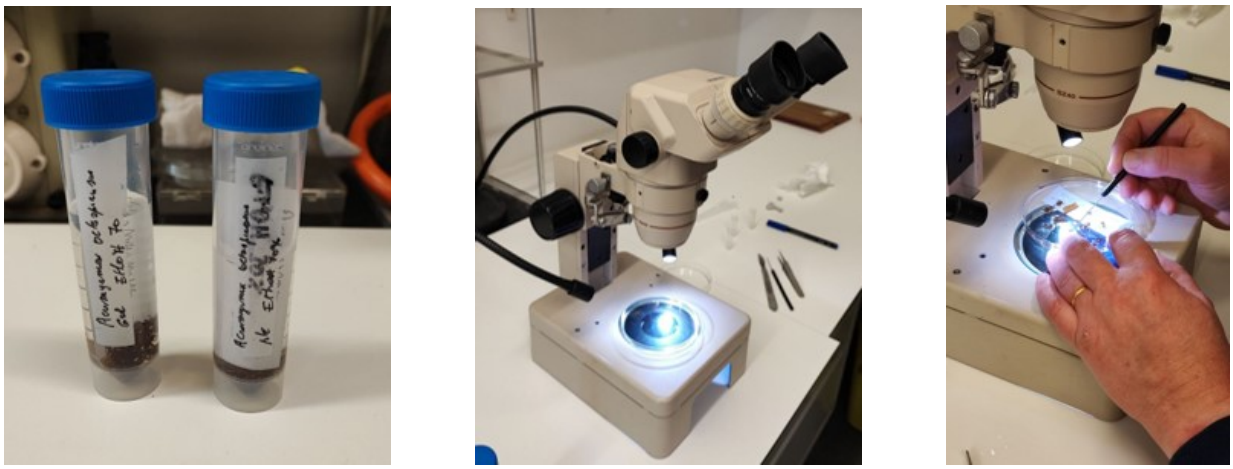

(a) **(b)** **(c)**

Figure 10: First steps in sample preparations: samples that were kept in absolute ethanol in Figure 10a are selected under optical microscope in Figure 10b and sectioned with tweezers in Figure 10c.

(a) **(b)**

Figure 11: Two different castes of *Acromyrmex octospinosus* workers under optical microscope: majors in Figure 11a and minors in Figure 11b.

To characterize the samples, it was necessary to embed them in resin: this allows for easier manipulation and makes it possible to cut them to expose the desired internal planes for SEM and nanoindentation. The resin used was an epoxy resin from the company Agar, it was prepared using reagents and volumes indicated in Table 1, along with their function, by adding them to a becker under a chemical hood and stirring with a magnetic stirrer to obtain a homogeneous solution.

Reagent	Volume[ml]
Agar 100 (resin)	4.75
DDSA (hardener)	1.99
MNA (hardener)	3.08
DMP 30 (accelerator)	0.12

Table 1: Reagents names and volumes needed to prepare epoxy resin.

The impregnation process for the samples involved two baths in absolute ethanol, each lasting at least twenty minutes, followed by two baths in propylene oxide, each lasting at least thirty minutes, carried out under a chemical hood due to the toxicity of the propylene oxide vapor. After this first step, the samples undergo four additional baths in mixtures of propylene oxide and epoxy resin, which were previously prepared following the proportions in Table 2. The duration of each bath is also reported in the same table.

Resin [ml]	Propylene Oxide [ml]	Time
1	2	1 hour
1.5	1.5	overnight
2	1	1 hour
2	0	overnight

Table 2: Impregnating solutions proportions and bath time.

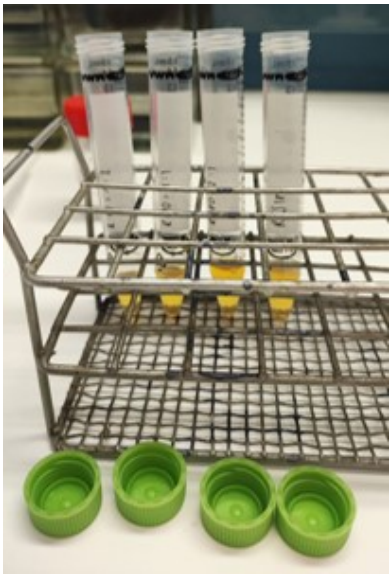

Figure 12: Resin and propylene oxide solutions used for the impregnation process.

The samples in the Eppendorf tubes filled with resin were placed inside a vacuum oven (Figure 13a) to remove residual propylene oxide and air by decreasing the pressure from 1000 millibars to 50 millibars. The oven has a trap chamber (Figure 13b) filled with liquid nitrogen to condense the propylene oxide toxic vapor. As the pressure decreases, gas bubbles form in the resin (Figure 13c) and after one hour from when the bubbles disappear, at around 50 millibar, the samples were ready to be positioned into silicone molds.

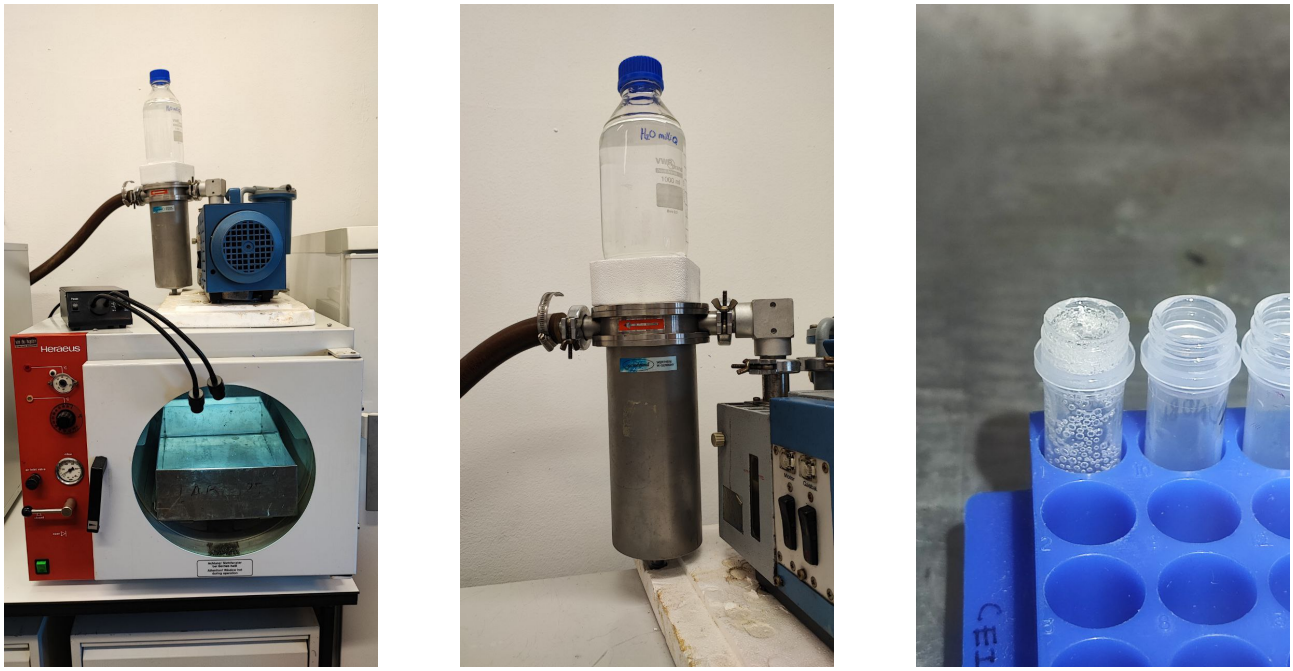

(a) **(b)** **(c)**

Figure 13: Overview of the vacuum oven setup and process. Figure 13a shows the outside of the machine, in Figure 13b the trap chamber for vapors is pictured and in Figure 13c it is possible to observe the gas being eliminated in the first Eppendorf tube.

The samples were then extracted from the Eppendorf tubes and placed into molds, as shown in Figure 14, in the desired orientation. After one week at 60 °C, the resin fully polymerized, and the samples were ready to be cut. Some samples moved inside the mold before the resin solidified so they were re-embedded in order to achieve the desired orientation.

Figure 14: Samples embedded in epoxy resin and oriented inside the molds.

In Table 3 the numbering of the samples, made accordingly to the mold they were in, is reported.

Mold number	Sample type
B1, B2, B3, B4, B5, B6	Majors mandible
C2, C3, C4,C5, C6, D1, D2, D3	Minord head
D4, D5, D6	Majors head

Table 3: Name of the samples according to the number of the mold they were in.

To cut the embedded samples and expose the surfaces for characterization we used a microtome with DiATOME diamond knives, pictures of the machine are reported in Figure 16b. The microtome allows for cutting slices of nanometric thickness suitable for analysis with transmission electron microscopy (TEM) and for obtaining flat and smooth bulk surfaces, which are fundamental to obtain reliable data from nanoindentation. The major samples were cut along three different planes (coronal, sagittal and transversal), while the minor samples were cut only cuts along the transversal plane due to their reduced dimension and to increase the reproducibility of the cuts. Slices approximately 70 nm thick were placed on a metal grid covered in Formvar for subsequent TEM observation, while bulk parts of the samples were used both for scanning electron microscopy observation and nanoindentation experiments.

(a) **(b)**

Figure 15: Ultramicrotome Reichert-Jung Ultracut E shown while cutting a sample in Figure 16a and as a whole in Figure 16b.

Formica rufa mandibles used for nanoindentation experiments were already embedded in epoxy resin and cut by staff in the biology department of University of Liège to expose the transversal plane for characterization.

2.1.1 Alternative sample preparation

An alternative method was tested alongside the one described in the previous section to evaluate the influence of the preparation technique on the values obtained for mechanical properties with nanoindentation tests. In this alternative method, two *Acromyrmex octospinosus* majors heads previously stained with rhodamine, were embedded in PMMA (polymethyl methacrylate) resin. The samples were then ground and polished to obtain a flat surface. The protocol followed is detailed in this section, with the results reported in Appendix D.

First, a staining solution containing rhodamine was prepared by stirring 40 grams of absolute ethanol and 0.25 grams of rhodamine with a magnetic stirrer for four hours on a hotplate, covered with aluminum foil to avoid rhodamine interaction with light. The ant heads were placed in two separate Eppendorf tubes and covered with the staining solution for three days, changing the staining solution daily. After three days, the rhodamine solution was discarded, and the Eppendorf tubes were filled with MMA (methyl methacrylate). After one more day, the MMA was discarded, and the Eppendorf tubes were filled with liquid PMMA and stored in the fridge for three days. To polymerize the resin, the Eppendorf tubes were placed in an oven for five days, starting at a temperature of 34 °C, increasing to 42 °C after two days, and to 50 °C after two more days. After PMMA polymerization, the Eppendorf tubes were cut perpendicular to their length using a wire diamond saw, and the samples were re-embedded in PMMA in a cylindrical mold with a 25 mm diameter to achieve the desired orientation.

Using the diamond wire saw, the PMMA cylinder was cut as close as possible to the ants mandibles. The samples were then ground until the surface of interest was exposed, using progressively finer carbide papers under ethylene glycol irrigation. Finally, the surfaces were polished with progressively finer diamond spray on silk cloths to obtain flat surfaces.

Observing them with an optical microscope (Figure 16) the samples look flat and adapt for nanoindentation. Additionally, rhodamine successfully penetrated into the samples, making it possible to study the structure of the mandibles through confocal microscopy.

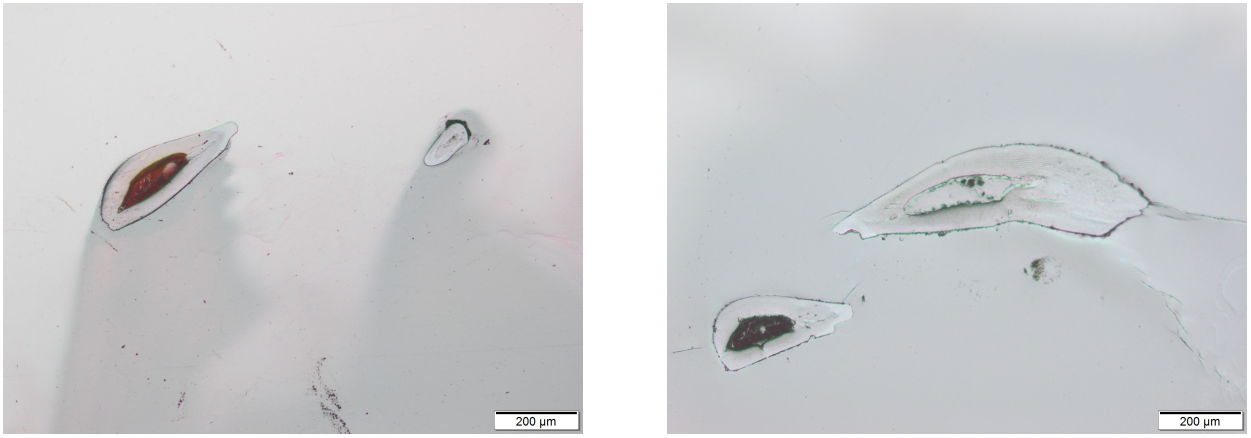

(a) **(b)**

Figure 16: Images at the optical microscope of the polished samples treated with rhodamine. The surface looks flat and with no visible defect, the slight pink color in both pictures means that the rhodamine successfully penetrated in the mandibles.

2.2 Digital Microscopy

A Keyence VHX-7000 digital microscope (Figure 17a), equipped with a stacking tool called 3D depth that allows for the stacking of multiple images to obtain a focused image of non-flat objects, was used. Images of *Acromyrmex octospinosus* heads were captured before embedding them in resin, an example of such images is shown in Figures 17b and 17c. Images of each sample were also acquired after resin polymerization.

(a) **(b)** **(c)**

Figure 17: Digital microscope Keyence VHX-7000 (17a) and pictures of major head (17b) and minor head (17c) obtained with 3D depth function.

2.3 MicroCT

MicroCT scans were performed on one major head and one minor head, using a Skyscan 1172 scanner (Figure 18a). Preparation for the scan was minimal: the heads were left to dry from the ethanol in which they were preserved and then glued on top of a cylindrical sample holder (with a drop of superglue for the bigger sample and with carbon tape for the smaller one) ensuring no movement during the scan. Scanning parameters were adjusted according to the sample size to achieve the best possible resolution. The raw data from the scans were processed using the softwares CTAn and CTVox.

(a) **(b)**

Figure 18: Overview of the microCT scan, Figure 18a from [9] shows the system and Figure 18b showing the sample holder used.

2.4 Scanning Electron Microscopy

A Tescan Clara Ultra-High Resolution scanning electron microscope (UHR SEM) was used to capture some images of the samples B1, B2, C3 and D4 (Table 3), which were previously cut with an ultramicrotome to expose the internal surface to characterize.

The samples were glued to cylindrical aluminum supports by putting a small amount of hot glue on top on the supports and heating them on a hot plate (Figure 19a) until the glue was melt. Tweezers were used to carefully manipulate samples without touching the exposed surfaces and to glue them vertically to their support. To prevent electron accumulation during analysis, a silver bridge (encompassing the aluminum support, the hot glue and the epoxy resin up to the surface of interest) was created by applying a solution of silver and isobutylmethylketone with an awl and allowing the solvent to evaporate under a chemical hood overnight. To further mitigate electron accumulation, the samples were coated with a thin layer of carbon using a carbon coater (Figures 19b and 19c). The analysis was conducted under high vacuum conditions with an electron accelerating voltage of 20 keV.

The SEM was utilized to capture images using both secondary electron (SE) and backscattered electron (BSE) modes, as well as for energy-dispersive X-ray spectroscopy (EDS) analysis to obtain X-ray spectra and elemental mapping of the sections. These techniques are illustrated in Sections 1.2.2 and 1.2.3).

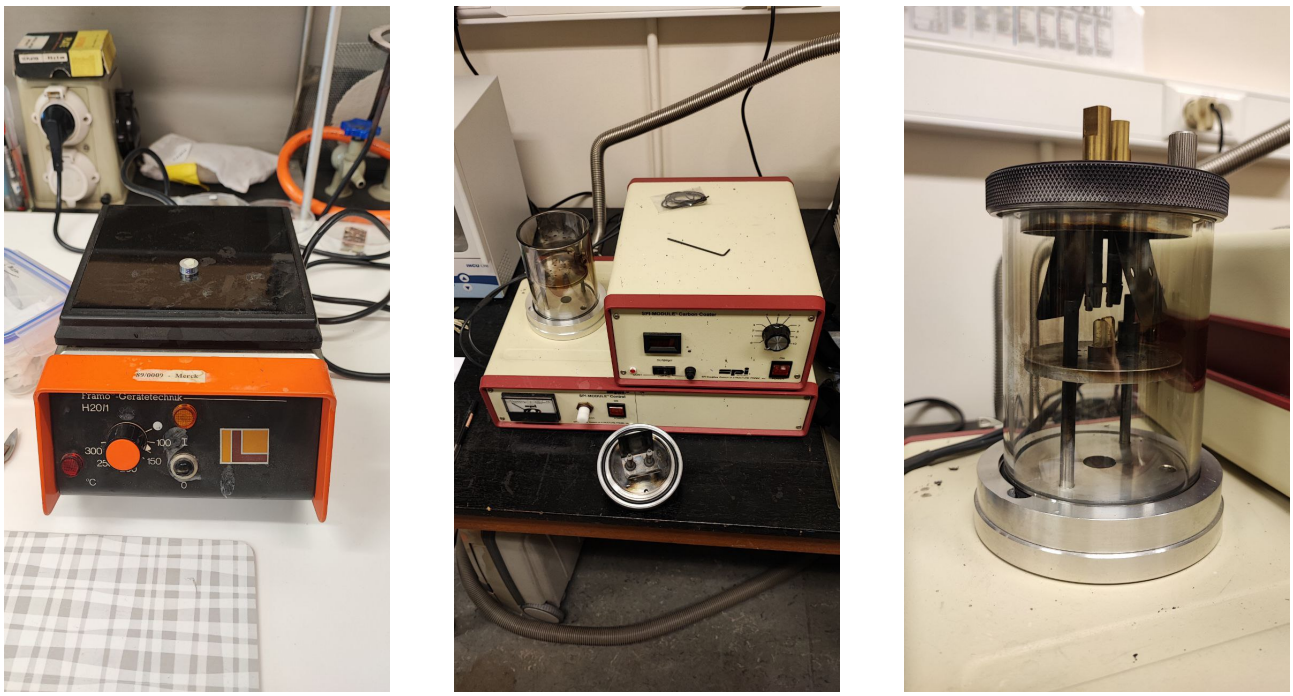

(a) **(b)** **(c)**

Figure 19: Instruments used to prepare samples for SEM observation. In Figure 19a the hot plate use to attach the sample to the aluminum support, in Figures 19b and 19c the carbon coater is shown along with the coating chamber.

2.5 Nanoindentation

The nanoindenter used was the Triboindenter TI 950 from Bruker, US. Two different conospherical diamond probes were used to perform the tests, one with a 5 μm tip radius and one with a 1 μm tip radius. Only samples with mandibles cut along the transversal plane were tested, due to the higher reproducibility of this cut.

Transducer calibration, optic-probe tip offset calibration, probe calibration and tip cleaning are critical aspects for every nanoindentation experiment, and will be briefly described in the following paragraphs before the description of the tests themselves.

Transducer calibration

The first step of any indentation experiment is the transducer calibration, made using the "Indentation Axis calibration" function of the nanoindenter software.

During an indentation test, the center plate (to which the probe is attached) of the transducer is driven into the sample surface. This movement of the center plate will cause a fluctuation in the Electrostatic Force Constant and if the transducer has not been properly calibrated a significant amount of error may be present in the results. TriboScan automatically accounts for changes in the Electrostatic Force Constant at large displacements. However, in order to make this correction, TriboScan must know the Plate Spacing of the transducer. The Plate Spacing and Electrostatic Force Constant are given by performing the Indentation Axis calibration (a contact-free actuation of the transducer) [22].

The Indentation Axis calibration is performed with the nanoindentation probe installed in the transducer and the transducer installed in the instrument. The nanoindentation probe performs an air indent using preconfigured specifications within the machine system, requiring no adjustments from the user. A triangular load function is employed, exerting a peak load of 600 μN resulting in the probe's displacement falling between 3.5-4.5 μm in air. If the displacement exceeds this range, force adjustments are made to ensure that the desired displacement range is achieved. During calibration, a graph is generated and compared with a fitted linear plot, the difference between the two is measured by the Root Mean Square Error (RMSE) value, which must be smaller than 5×10^{-5} in order for the calibration to be considered successful, if the RMSE value exceeds this threshold the calibration process must be repeated.

Optic-probe tip offset calibration

Hysitron TI series instruments are optically driven instruments. A properly calibrated instrument allows to optically focus the camera on an area of interest, define a sample boundary and perform a test. In order to accomplish this task, TriboScan needs to record the distances in the X, Y, and Z axis between the center of the optical focal plane and the probe. This calibration is required if any of the system hardware components related to the distance of the probe or optics has changed. To perform the manual calibration 7 indents in an "H pattern" shape are performed on an aluminum sample with a peak force high enough to see the indenter traces

but not too high to avoid excessive penetration in the sample. The user must then place the H in the center of the field of view as shown in Figure 20.

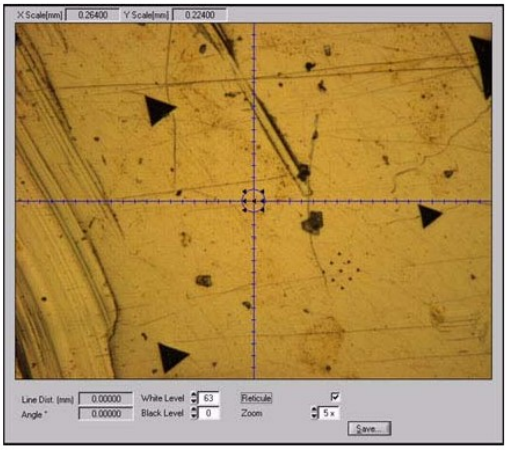

Figure 20: H pattern for the optic-probe tip offset calibration. Figure from [16].

Probe calibration

Probe calibration is fundamental to establish the correlation between penetration depth (h_c) and contact area (A) or contact radius (a). Performing a probe calibration for each probe will compensate for non-perfect probe shape. The probe radius of curvature and normal dulling of the probe can both be corrected by recalibrating the probe.

Calibration protocols are different for different nanoindentation techniques.

For quasi-static nanoindentation the protocol is described in the nanoindenter user manual [22]: to determine the area function, a series of indents at various contact depths (varying normal loads) are performed in a sample of known elastic modulus (typically fused quartz) and the contact area A is calculated. A plot of the calculated area as a function of contact depth is created and the TriboScan software fits the A versus h_c curve to the sixth order polynomial in Equation 9.

$$A = C_0 h_c^2 + C_1 h_c^{1/2} + C_3 h_c^{1/4} + C_4 h_c^{1/8} + C_5 h_c^{1/16} \tag{9}$$

The load function used for the probe calibration is a load control load function with a 5 second load time, 2 second hold time and a 5 second unload time. A 10 by 10 array is used to increase the accuracy and reliability of the calibration with loads decreasing by a fixed amount from 10000 μN down to around 100 μN.

For stress-strain experiments Fused Quartz is indented using a basic trapezoid load function with decreasing loads for each indent, ranging from 1500 μN to 10 μN across two grids of $8\times8 points with spacing of 6\mu$m between indents. The data is analyzed using TriboScan software and a Matlab script to derive an equation correlating the contact radius and penetration depth,

represented by Equation 10. The coefficients of the equation are determined through analysis of the calibration data.

$$a = E_0(1 + h_c)^{E_1} \tag{10}$$

Tip cleaning

It is important to clean the tip between different tests to remove any possible dirt or debris present on it. Two indents are performed on an aluminum sample using a trapezoidal load function with a peak load of 10000 μN, between the two indents, the tip is moved 10 μm along the horizontal axis and 10 μm along the vertical axis, maintaining a setpoint of 5 μN. The high load value used for the two indents ensures sufficient penetration into the aluminum to effectively clean the tip.

2.5.1 Scanning Probe Microscopy (SPM)

Before any indentation experiment, SPM is performed to evaluate the topography of the area to be indented. The probe-transducer combination is mounted on a high-precision 3-axis tandem tube piezo scanner. The X-Y piezo directions raster scan the sample surface, while the Z displacement of the piezo maintains a consistent imaging force.

This synchronised X-Y-Z movement produces a high resolution topography map of the surface. The error in the actual load supplied to the sample relative to the setpoint (measured by the transducer) is the gradient image. Topography images are useful for physical measurements of the surface, whereas gradient images are usually more visually clear. In this work, only the topography images are used to make comparisons and calculations.

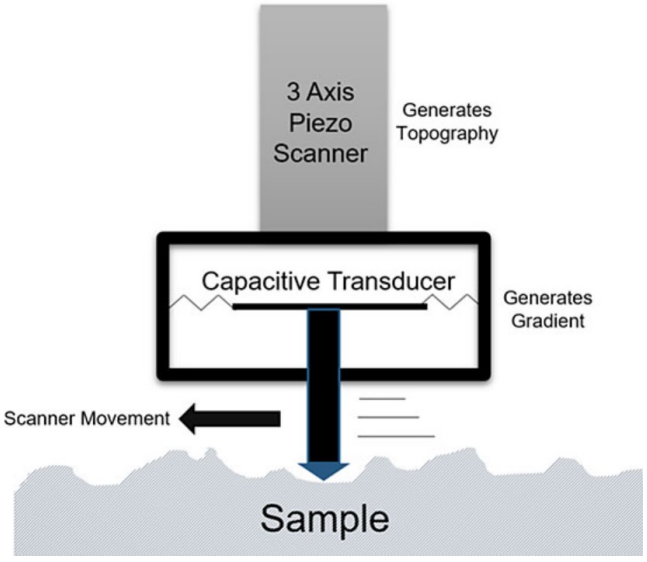

Figure 21: SPM working mechanism illustration [23].

To obtain appropriate SPM images the following parameters must be adjusted:

- Scan rate [Hz]: varies depending on the desired image resolution. Lower scan rates require more time but result in higher image resolution, so it is important to find a good compromise, in this work we used scan rates from 0.25 to 1.
- Scan size [μm]: defines the dimension of the square area of the sample to scan, in this work it ranges from 8 to 30.
- Setpoint [μN]: specifies the force applied to the sample when the probe is in contact with it. For this analysis the value is set to 2.

2.5.2 Quasi-Static Nanoindentation

Quasi-static nanoindentation was employed to assess indentation hardness and reduced modulus, also called indentation modulus, of various area of the sample. Some tests were conducted using a 5 μm and some using a 1 μm tip radius conospherical diamond probe. Since the tip radius is a parameter that could play a role in the obtained results, we decided to consider only the tests performed with the 1 μm tip radius in the results.

Load evaluation

An initial test was conducted on the first examined sample to determine the most appropriate loading conditions for the material. Using the 5 μm tip, nine indents were made on a $3\times3 grid with 6\mu$m spacing between indents, using a load incrementally increasing from 200 to 2000 μN. Based on the results of this test, subsequent quasi-static measurements were performed with a 1500 μN load for the 5 μm tip and 500 μN load for the 1 μm tip. This choice is motivated by the fact that to obtain the same penetration depth in the sample, an higher load is needed for an higher tip radius.

Quasi-static nanoindentation protocol

The area to be indented was selected by looking at it with the optical microscope of the nanoindenter. Subsequently, an SPM at high scan rate (1 Hz) was performed to verify that the area was sufficiently flat, a second scan at a lower scan rate (0.25 Hz) was then conducted to obtain an image with an higher resolution from which the indents locations were chosen. Either an arrayscript (Figure 22b) or a clickscript (Figure 22a) was used to select the indentation locations within the imaged area. For each test, the indents locations were saved in a BMP file, like the ones shown in Figure 22.

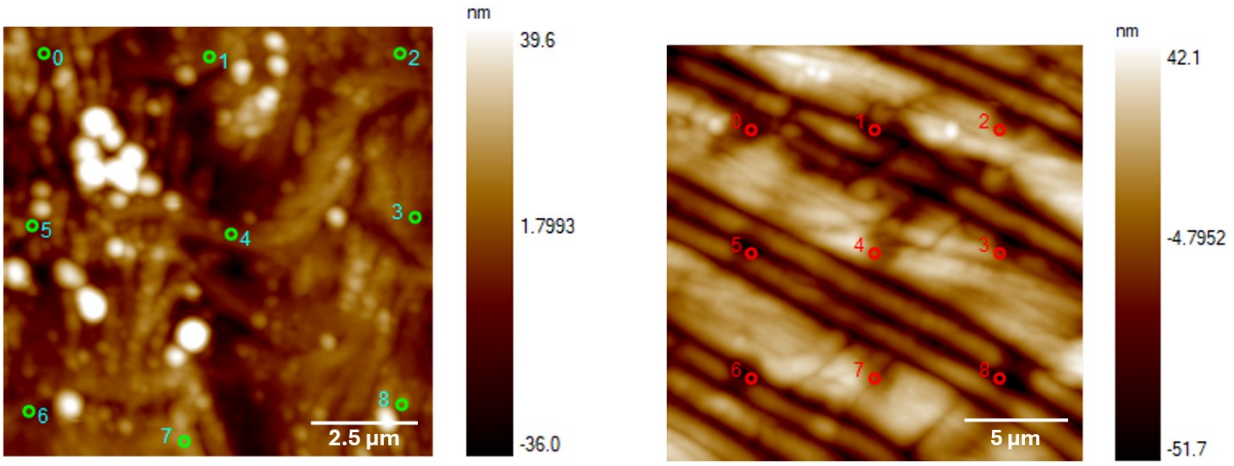

(a) **(b)**

Figure 22: Indents locations either selected manually with a clickscript (Figure 22a) or automatically with an arrayscript (Figure 22b).

A trapezoidal load function with maximum load depending on the tip radius was selected and the nanoindentation test was conducted on the selected locations. An SPM post nanoindentation was performed to see if the mark of the indents was visible on the sample, most of the time this was not the case. The indentation data were processed using the TriboScan software.

2.5.3 Stress Strain Nanoindentation

The protocol for this test is similar to the one described for quasi-static nanoindentation, with two major differences: the load function and data processing. The load function is shown in Figure 23, with a maximum load of 200 μN and in Open Loop mode.

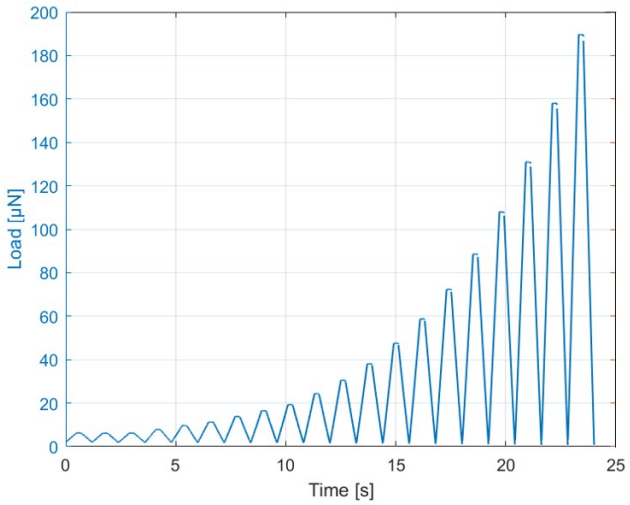

Figure 23: Stress strain load function. Starting with 3 indents at a 5 μN and increasing progressively until the maximum load is reached.

For some experiments a preload cycle of 20 μN was used to see if the results would be more homogeneous, the results of this method are presented in Appendix B.

To plot the stress-strain curves and analyze the data, some Matlab scripts, already consolidated by previous studies, have been used. The code plots the stress-strain curves relative to the desired indents having the load and depth data obtained from the nanoindenter as inputs.

2.5.4 Wear test

To perform the wear test, after the initial SPM scan to evaluate the topography of the selected location, the parameters described in Section 2.5.1 were modified: the setpoint was increased to remove material from the samples (we tested setpoints from 300 μN to 700 μN), the scan rate was adjusted according to the scan size to maintain the tip the velocity at 100 μm/s, and the scan size was reduced (depending on the available area) to observe the difference in height of the tested area before and after the test. After the wear test, an SPM scan with the same size as the initial one was performed. The topography images obtained with the SPM scans were saved as txt files using the software Triboview and analyzed with the software ImageJ to measure the mean height of the same area before and after wear tests and evaluate the wear resistance based on the wear height, measured as the difference of the two mean heights.

2.5.5 Nanoindentation samples

Nanoindentation was performed only on one sample for each type of ant, cut along the tranversal plane. Pictures obtained at the optical microscope of the nanoindenter before the experiments are reported in Figure 24.

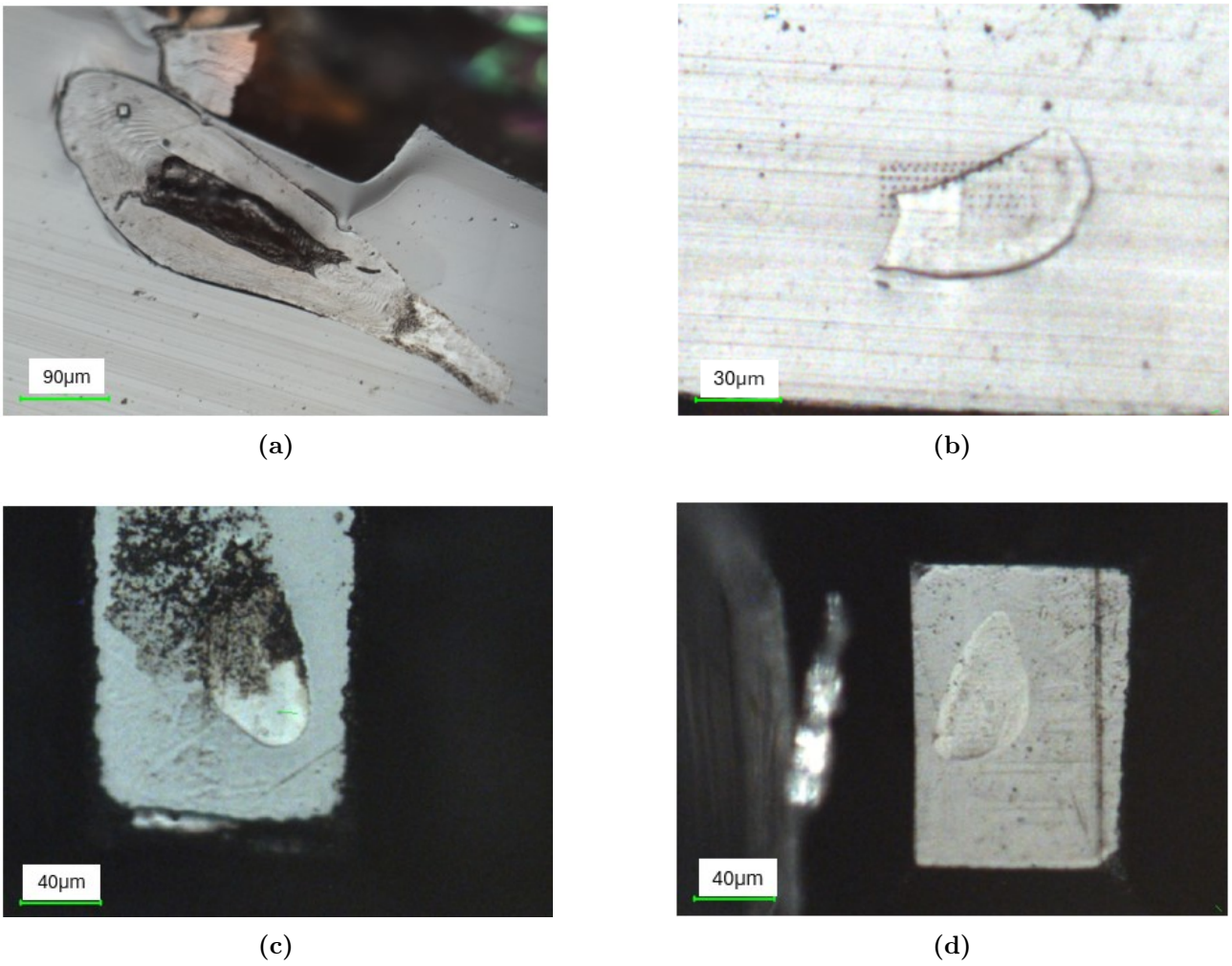

(a) **(b)**

(c) **(d)**

Figure 24: Images of the different samples used for nanoindentation: in Figure 24a sample D4 (*Acromyrmex Octospinosus* major), in Figure 24b sample C3 (*Acromyrmex Octospinosus* minor), in Figure 24c sample E (*Formica Rufa* major), in Figure 24d sample G (*Formica Rufa* minor).

3. Results

The purpose of this section is to present all the results obtained with the different characterization techniques, it is divided in three main sections: imaging, composition and mechanical properties.

3.1 Imaging

This section presents images of the samples acquired through optical digital microscopy, 3D reconstructions of the heads of the two different workers castes of *Acromyrmex octospinosus* obtained with microCT, and it is concluded by SEM images of different internal planes of the samples.

3.1.1 Digital microscopy

Pictures of front and back sides of one major worker ants are reported in Figure **??**, in Figure 26 the same is done for a minor worker. The images obtained thanks to the 3D depth technology allow to have a focused image of a curved object, making it possible to observe small details. It is interesting to compare the two sets of images and observe the differences in morphology between the two workers castes that can be associated to the different function they perform in the colony.

- Dimension: the head and the mandibles of minors are considerably smaller than the ones of majors, the major's head being almost four times larger than the minor's one.
- Shape: the shape of the heads is very similar, the shape difference is more interesting in the mandibles, those of the minors look flatter and sharper compared to the majors ones, the teeth looks also less worn.
- Color: majors samples appear darker than the minors ones, the mandibles of both castes present a darker teeth lining, corresponding to the tanned cuticle, tanning being the process of insects cuticle hardening by loss of water and creation of crosslinkings between proteins.

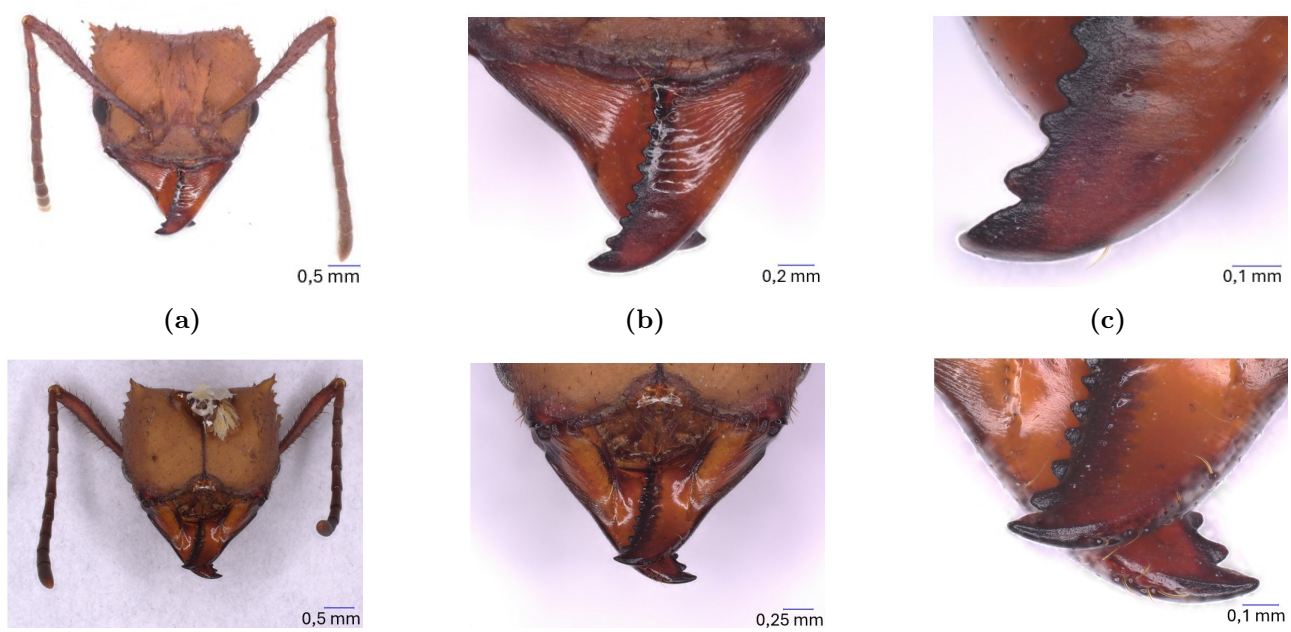

(a) (b) (c)

(d) (e) (f)

Figure 25: Major head and details of the mandibles. In Figures 25a, 25b and 25c the front of the sample is shown, allowing to see the curved shape of the mandibles crossed one on top of the other and the thin dark teeth lining. In Figures 25d, 25e and 25f the back of the sample is visible, and it is possible to observe the mouth of this ant and the attachment of mandibles to the head.

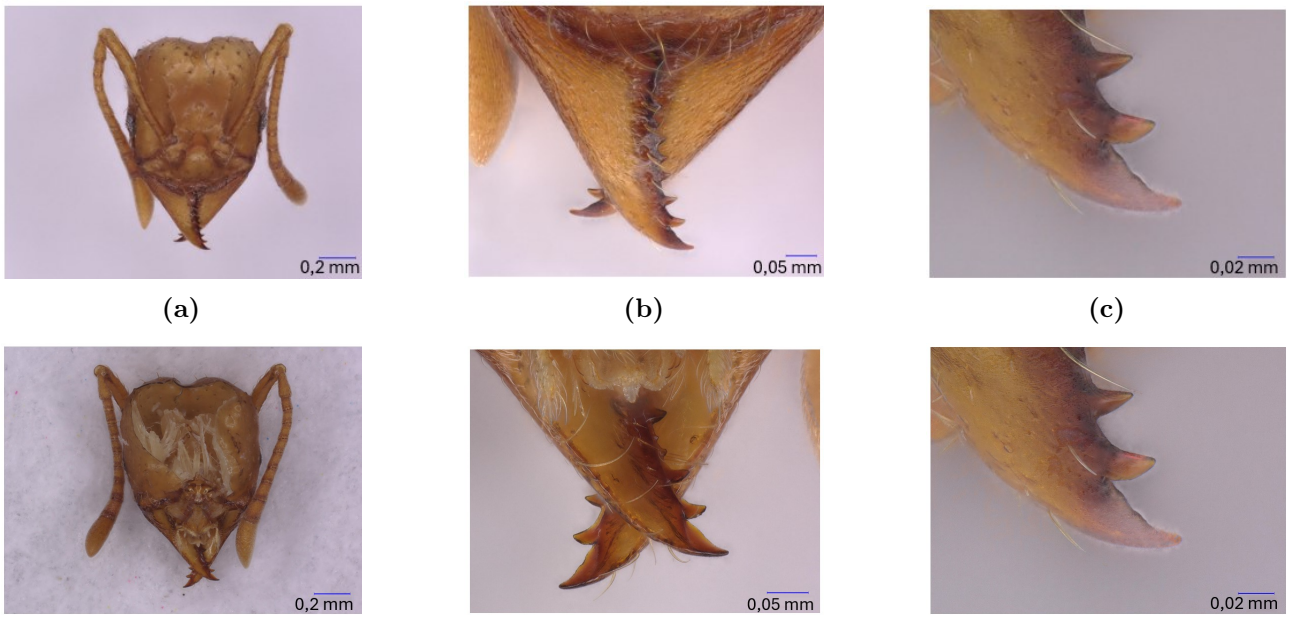

(a) (b) (c)

(d) (e) (f)

Figure 26: Minor head and details of the mandibles. In Figures 26a, 26b and 26c the front of the section is shown with increasing magnification. In Figures 26d, 26e and 26f the back of the head and mandibles is shown, teeth present different dimension and shapes.

3.1.2 MicroCT

This section presents both raw acquisition images from the CT scan and reconstructed images generated from the 2D slices using the software CTVox.

The images in Figure 27 are examples of the multiple projections acquired as the sample rotates during the 3D reconstruction process described in Section 1.2.1. They have scalebar measuring 1 mm, evidencing the dimensional difference between the two studied workers castes.

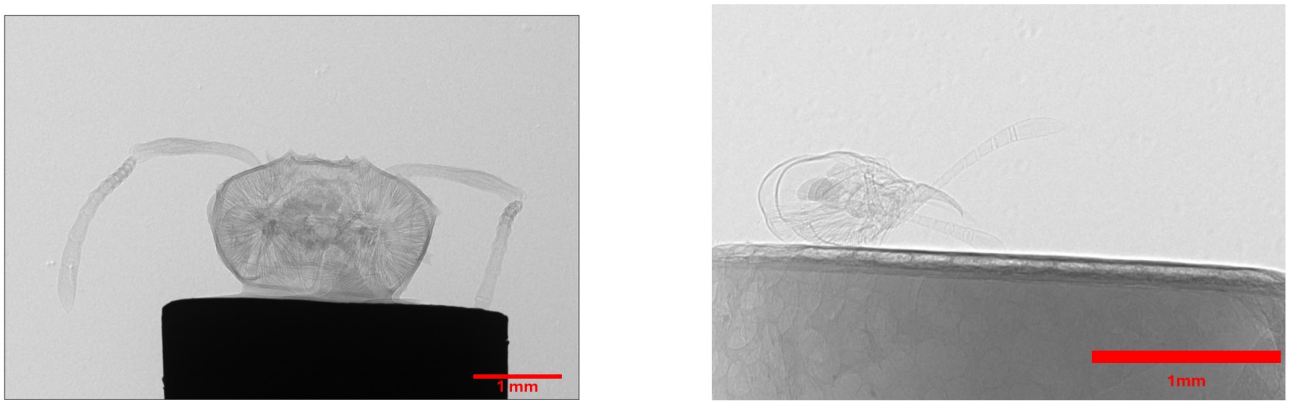

(a) **(b)**

Figure 27: Scan projection radiographs of *Acromyrmex octospinosus* major (Figure 27a) and minor (Figure 27b) ants. These are individual X-ray projections that combined with many others taken at different angles allow to obtain a 3D reconstruction of the samples.

In Figure 28 the heads of the two studied workers castes are compared, the difference in dimension and morphology can be easily appreciated.

In Figure 29 the morphological differences in mandibles of majors and minors workers are highlighted, for this comparison, the mandibles were isolated from the heads by manually segmenting the individual 2D slices using the software CTAn, and the results were visualized using CTVox.

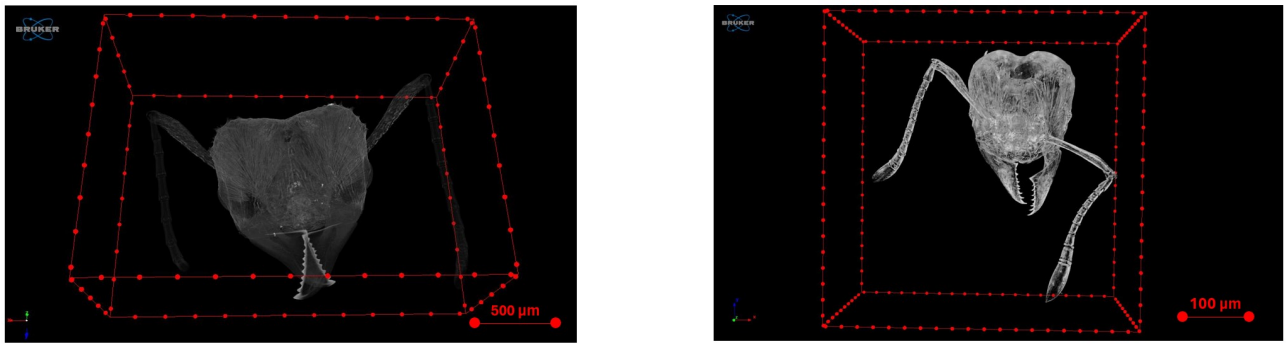

(a) **(b)**

Figure 28: Reconstructions of *Acromyrmex octospinosus* ants head using the software CTVox. Major's head in Figure 28a and minor's head in Figure 28b.

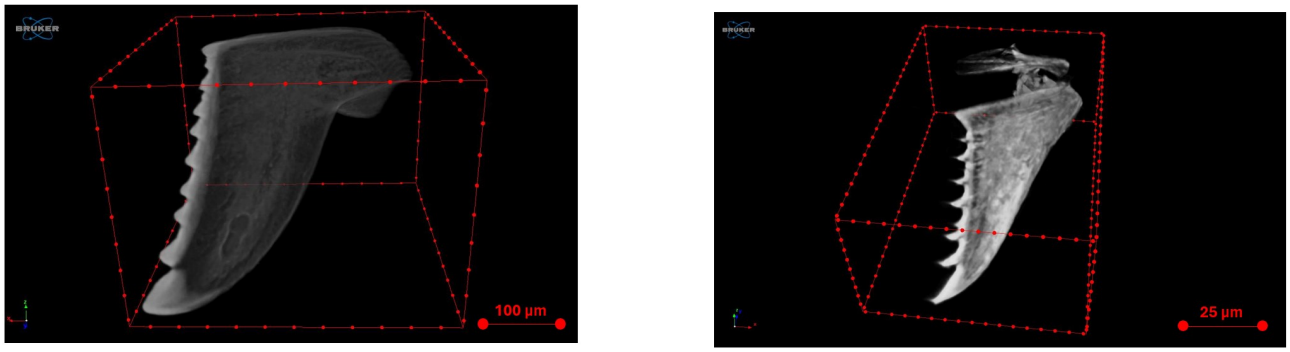

(a) (b)

Figure 29: Reconstructions of *Acromyrmex octospinosus* ants mandibles using the software CTVox. Major's mandible in Figure 29a and minor's mandible in Figure 29b. It is possible to observe a local higher density of the cuticle in correspondence of the teeth lining, which correspond to a lighter color in the image. The teeth in the minor caste look sharper and less worn.

3.1.3 Scanning Electron Microscopy

In this section, samples are referenced by the mold in which they were embedded, with corresponding details about the samples and the cutting planes provided in Table 4.

Mold number	Caste	Cutting plane
D4	Major	Transversal
C3	Minor	Transversal
B1	Major	Coronal
B2	Major	Sagittal

Table 4: Samples castes and cutting plane.

The images captured in backscattered electron (BSE) mode highlight contrasts between areas of different atomic numbers, as discussed in Section 1.2.2. Higher atomic numbers result in increased emission of backscattered electrons, which appear as lighter regions in the images. For instance, zinc, with an atomic number of 30, contrasts with the primary elements of the cuticle (carbon, nitrogen, and oxygen, with atomic numbers of 6, 7, and 8, respectively) resulting in lighter areas where zinc reinforcement is present. In all images, the detachment of the cuticle from the resin is evident. This detachment occurs because one of the primary functions of the cuticle is to serve as a barrier to permeability.

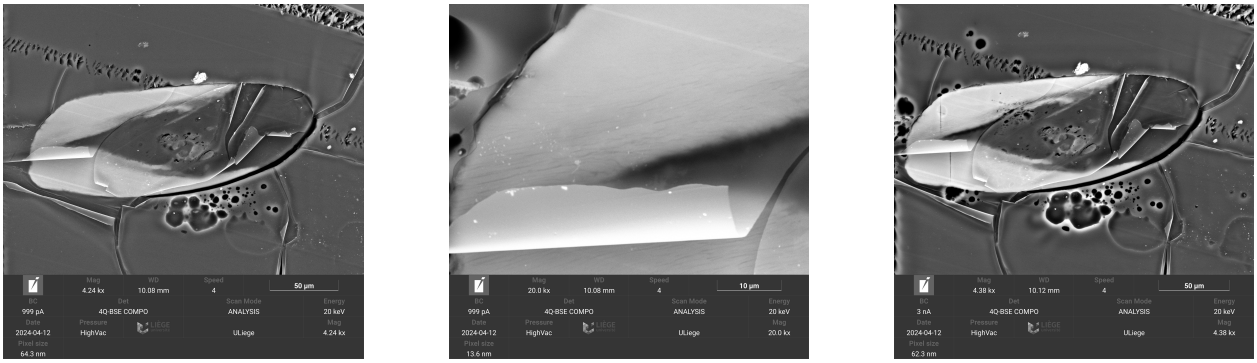

(a) **(b)** **(c)**

Figure 30: Pictures of sample D4 in BSE mode: Figure 30b shows detachment of the carbon coating from the sample's surface, in Figure30c beam induced damage appears as holes.

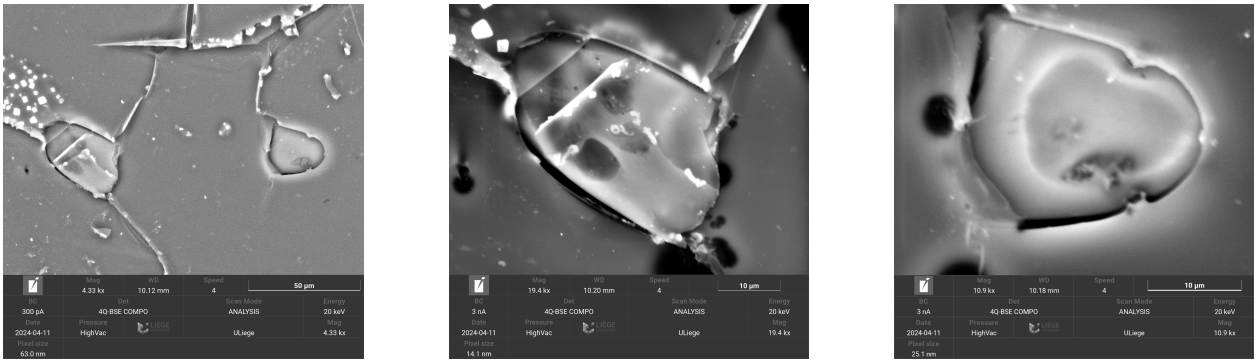

(a) **(b)** **(c)**

Figure 31: BSE images of sample C3: in Figure 31a cracks in the resin are evident, Figure 31c clearly shows the detachment between the resin and the cuticle.

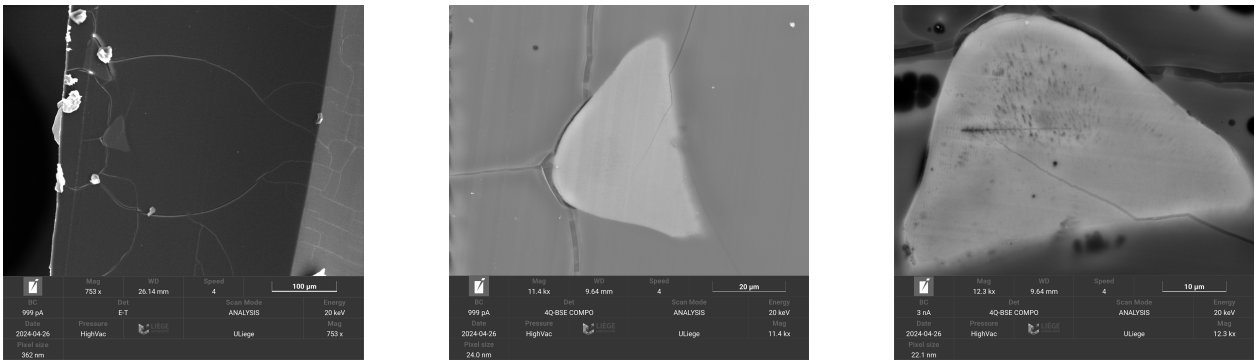

(a) **(b)** **(c)** B1

Figure 32: BSE images of sample B1: Figure 32c highlights the pores in the teeth, enlarged due to electron beam damage.

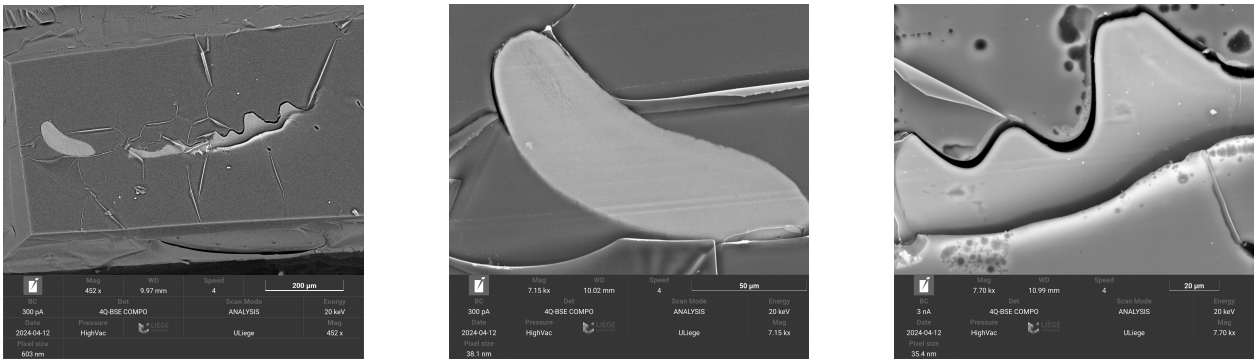

(a) **(b)** **(c)**

Figure 33: BSE images of sample B2: Figure **??** shows the interior of various teeth, Figures 33b and 33c show higher magnification details and the evident detachment between cuticle and resin.

3.2 Composition

Energy dispersive spectroscopy (EDS) provided insights into the distribution of selected elements within the mandibles samples. The following figures qualitatively show the spatial localization of zinc (Zn), chlorine (Cl), and, in some cases, phosphorus (P).

Chlorine is primarily associated with the resin used for embedding the samples, while phosphorus indicates the presence of cellular material, as seen in Figure 34b. Zinc is represented by two distinct peaks: the K peak and the L peak. When Zn is indicated in the pictures it corresponds to the K peak of the zinc, while when Zn is reported in the images it actually indicates the L peak of Zn, as the peak relative to Na has the same energy of the L peak of Zn.

The difference between zinc-reinforced and non-reinforced cuticle regions is only observable in Figure 34b, since the other samples were sectioned near the tooth tip, where zinc is uniformly distributed through the whole section. To better visualize the differentiation between these two regions, deeper cuts would be required.

The naming convention for samples in this section follows that of the previous one, with sample identifiers provided in Table 4.

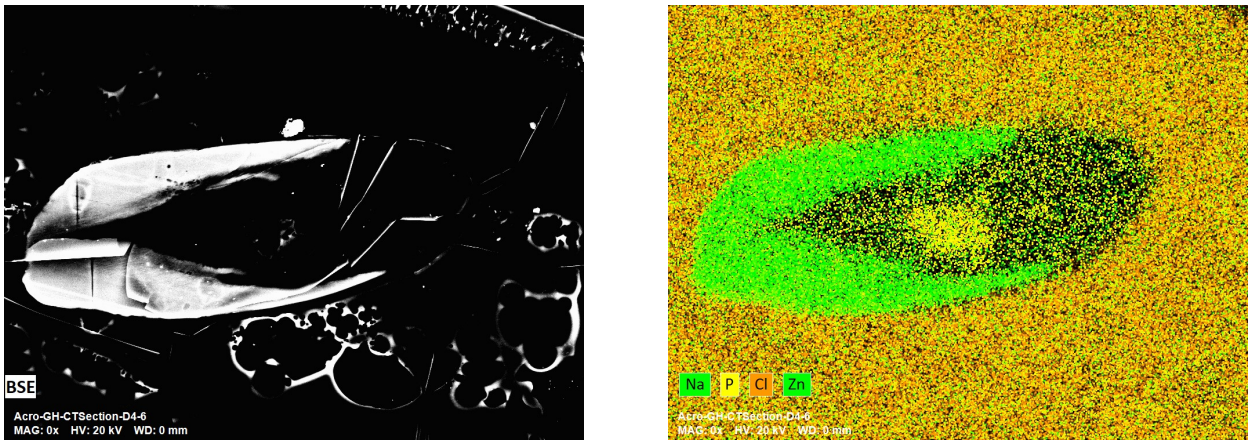

(a) **(b)**

Figure 34: BSE image of the mapped area (Figure 34a) and elemental mapping of Zn, P and Cl in sample D4 (Figure 34b).

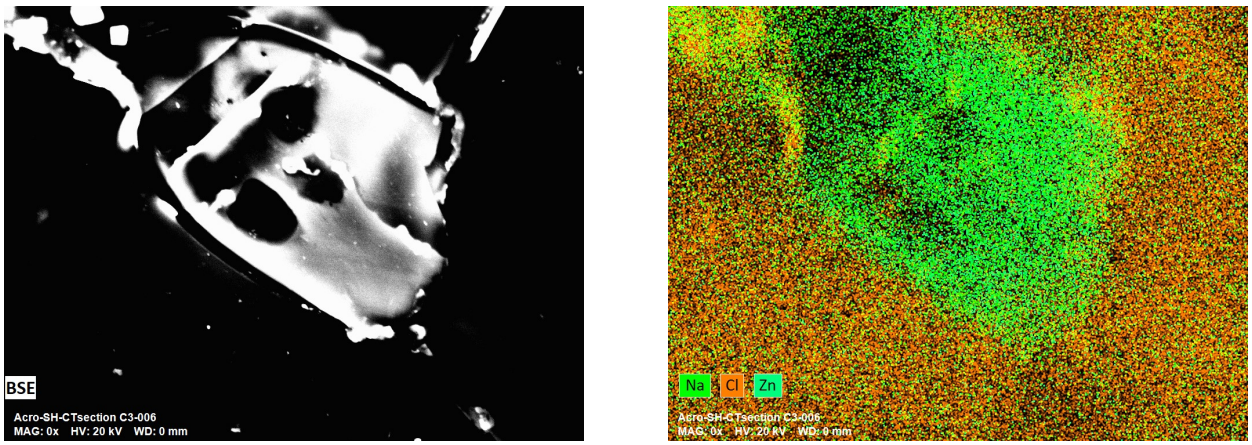

(a) **(b)**

Figure 35: BSE image of the mapped area (Figure 35a) and elemental mapping of Zn and Cl in sample C3 (Figure 35b).

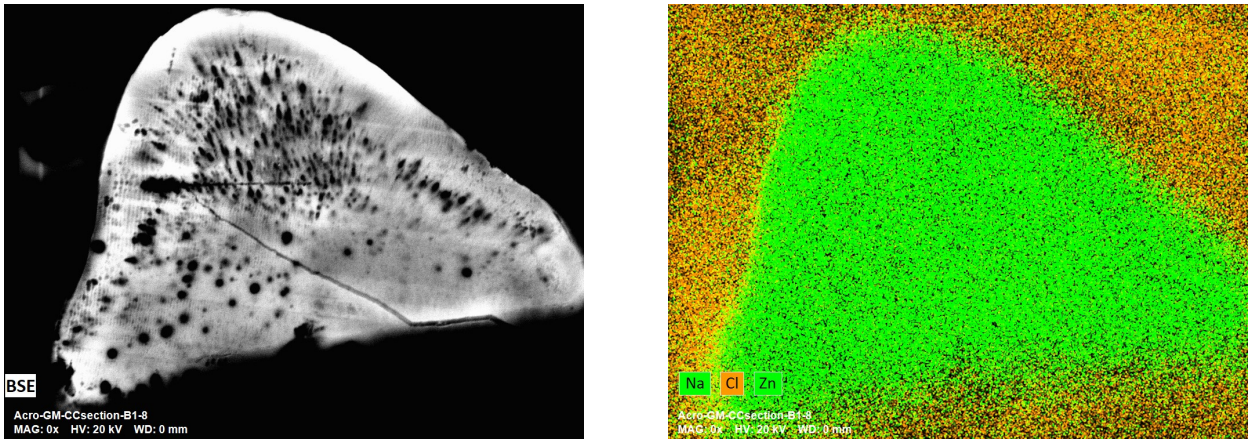

(a) **(b)**

Figure 36: BSE image of the mapped area (Figure 36a) and elemental mapping of Zn and Cl in sample B1 (Figure 36b).

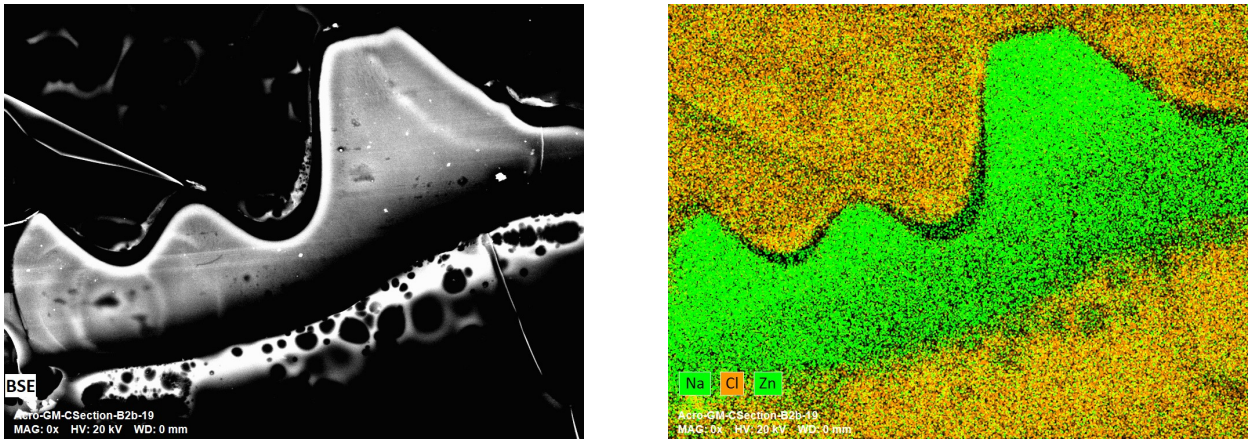

(a) **(b)**

Figure 37: BSE image of the mapped area (Figure 37a) and elemental mapping of sample B2 (Figure 37b).

3.3 Mechanical properties

This section presents the central results of this work, displaying all the findings obtained using various nanoindentation techniques.

For quasi-static nanoindentation and wear tests the results were achieved using a conospherical diamond probe with a tip radius of 1 μm. For the stress-strain nanoindentation, a different conospherical probe with a tip radius of 5 μm was used. All the samples were tested on the transversal plane, which is the one shown in Figure 38.

The results are presented sample by sample for each technique. Different factors can affect the numerical values obtained for mechanical properties, making direct comparisons between them complex.

Figure 38: Red line corresponding to the transversal cut performed on the samples. Image of a sample of *Acromyrmex octospinosus* major worker embedded in epoxy resin taken at the digital microscope.

3.3.1 Quasi-Static Nanoindentation

This section contains the results obtained through quasi-static nanoindentation experiments, in particular indentation modulus (also called reduced modulus) and indentation hardness obtained from the analysis of load-depth curves on different areas of various samples.

In the images illustrating the locations of the indents the differences in surface topography of the tested areas are visible. The topography images were obtained with SPM as described in (2.5.1).

Since the indentation modulus and hardness values for the different samples and areas are displayed using boxplots a brief explanation of these graphs components is provided to facilitate better understanding of the results.

Boxplots

The boxplots used in this study summarize the distribution of the data using key components that are illustrated in Figure 39:

- **median**: indicated by a line that splits the box in two, half of the data are above this value and half of the data are below. Can be called Q2
- **average**: indicated by an x
- **lower quartile**: the value below which 25% of the data are, also called Q1
- **upper quartile**: the value below which 75% of the data are, also called Q3
- **lower extreme**: lower value of the dataset excluding outliers
- **upper extreme**: higher value of the dataset excluding outliers
- **outliers**: indicated by circles, values that fall out of the Q1-1.5×IQR or Q3+1.5×IQR where IQR = Q3-Q1

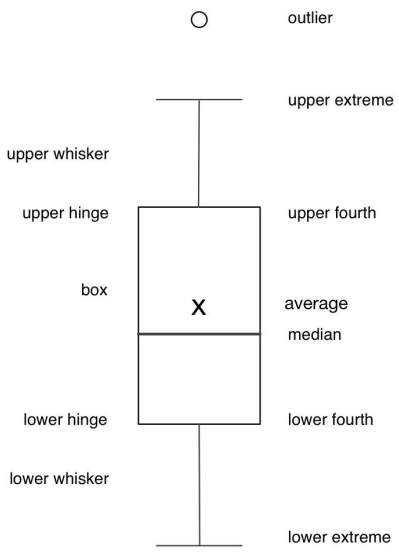

Figure 39: Schematic representation of a generic boxplot. Labels on the left correspond to the graphic elements, while those on the right indicate the associated summary statistics. Figure adapted from [24].

Acromyrmex octospinosus major (D4)

Two different topographies are observed by looking at the clickscripts of the two different areas of sample D4 shown in 40, one corresponding to the the zinc-reinforced area and one to the non-reinforced part of the mandible. The data regarding the 9 indents performed on each of the

two areas are shown in the boxplots in Figure 41, from the graphs it is evident that indentation modulus and hardness are notably higher in the zinc-reinforced area.

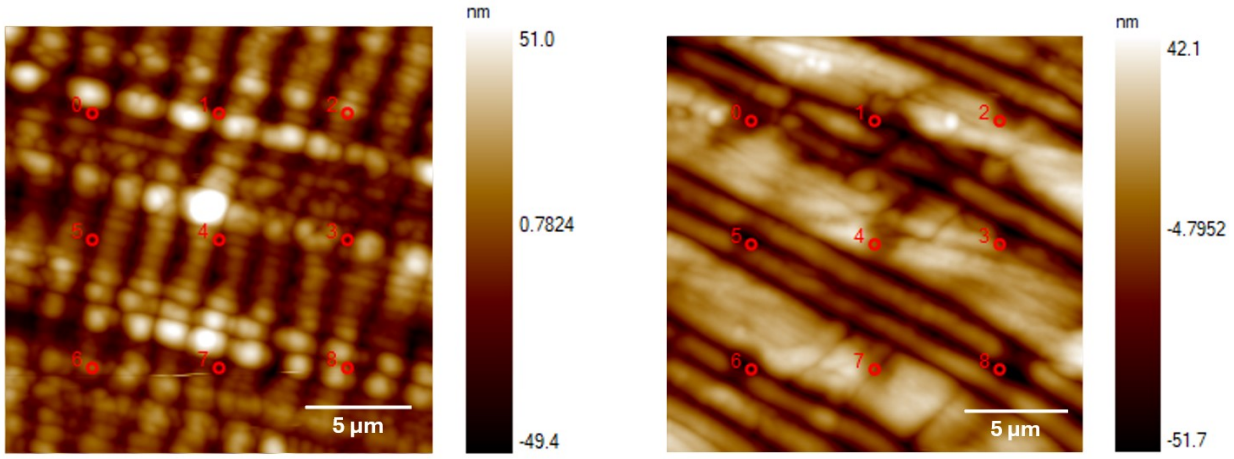

(a) **(b)**

Figure 40: Arrayscripts of the indented areas on topographical images obtained with SPM. Zinc-reinforced area in Figure 40a and non-reinforced area in Figure 40b.

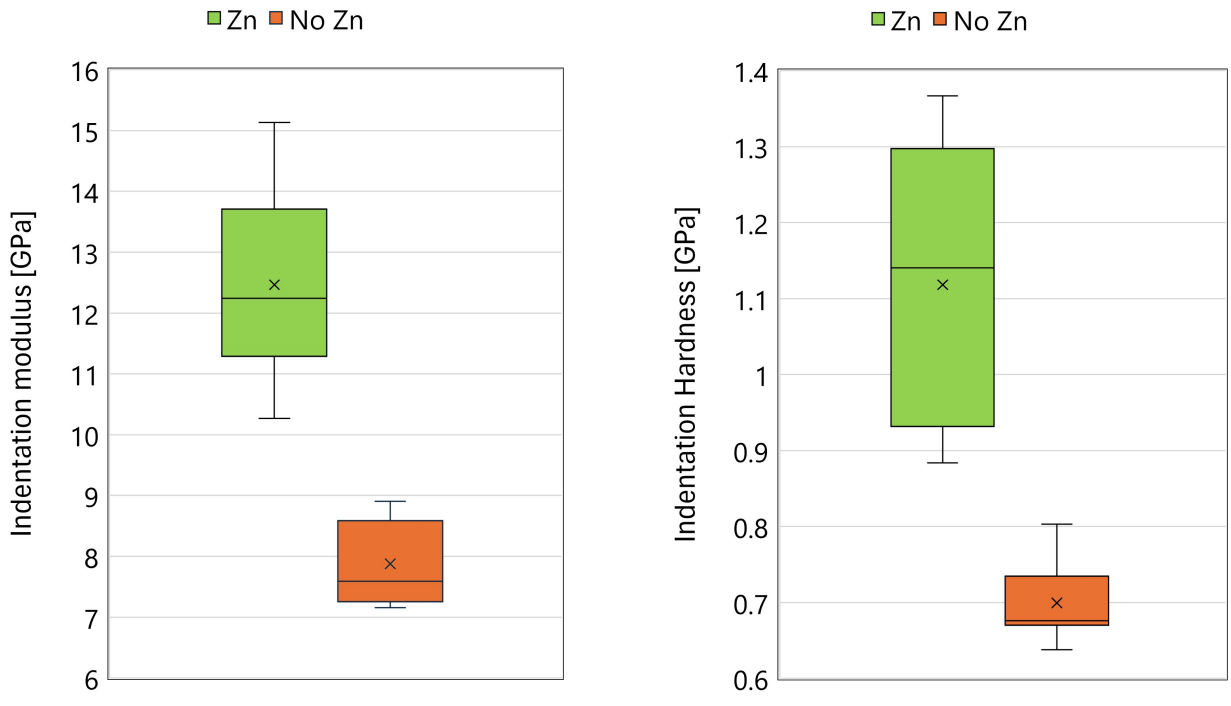

(a) **(b)**

Figure 41: Boxplots of reduced modulus and hardness obtained from quasi-static nanoindentation on two different areas of an *Acromyrmex octospinosus* major mandible. The variability of data distribution in the zinc-reinforced area is bigger, with values of indentation modulus and hardness reaching significantly high values.

Acromyrmex octospinosus minor (C3)

The mechanical properties of this sample were mapped by performing a series of equally spaced indents (3 μm) on an area encompassing different regions of the mandibles and some resin. This area is highlighted with a red rectangle in the optical microscope image and shown in the arrayscript in Figures 42. The 2D maps of reduced modulus obtained from these indents is displayed in Figure 44a, and the hardness mapping is shown in Figure 44b. The zinc-reinforced area of the mandible is harder and stiffer than the non-reinforced cuticle of the same sample.

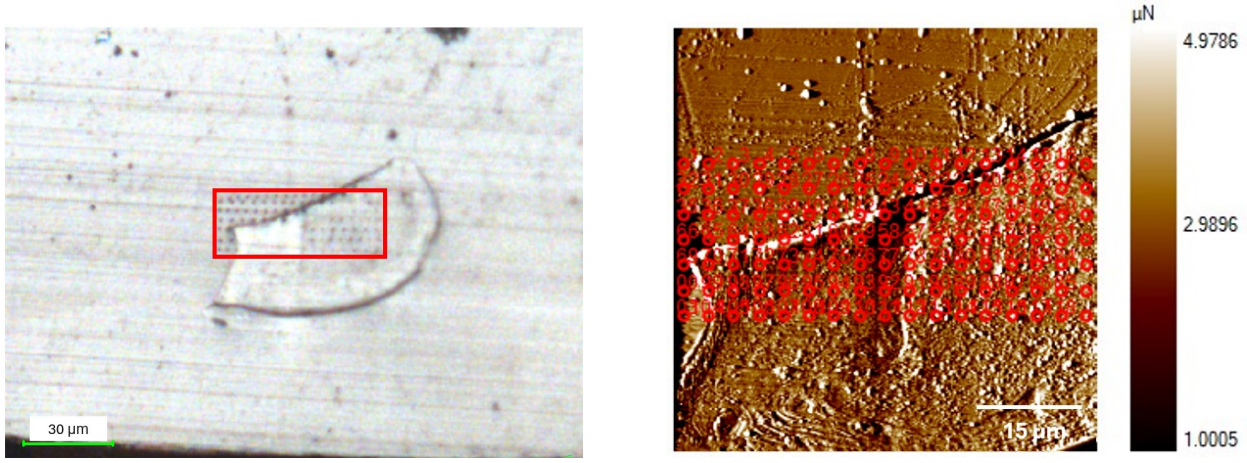

(a) **(b)**

Figure 42: Images of the mapped area of sample C3. In Figure 42a an optical image of the sample C3 after indentation, the indents are visible in the area inside the red rectangle. In Figure 42b the arrayscript of the indented area for mechanical properties 2D mapping visualized on a gradient forward image obtained with SPM.

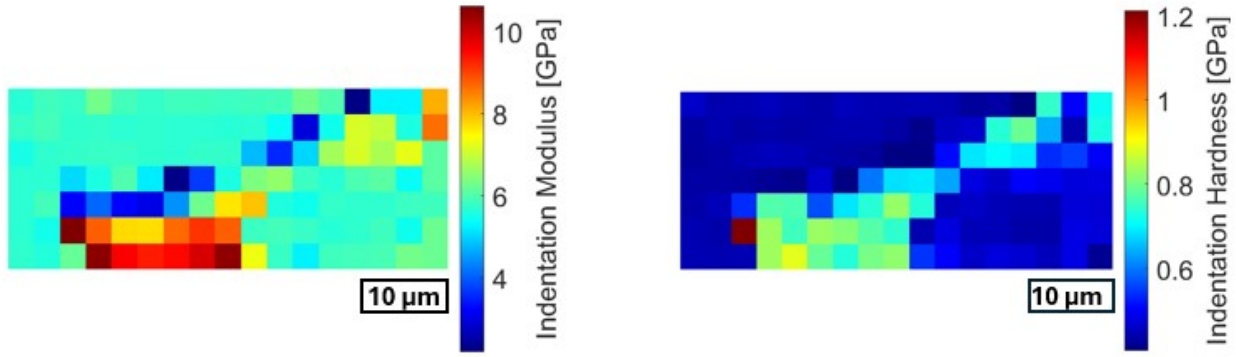

(a) **(b)**

Figure 43: 2D mapping of indentation modulus (43a) and of indentation hardness (43b. The elastic properties are significantly higher in the zinc-reinforced area and the values are close to the ones of epoxy resin in non-reinforced cuticle.

To maintain consistency with the analysis performed on the sample of *Acromyrmex octospinosus* major worker, values of indentation modulus and indentation hardness were taken from 9 indents in each zone (reinforced with Zn, non-reinforced, and resin) to plot the boxplots shown in Figure 44. Both the values of indentation modulus and indentation hardness displayed in the graphs are higher in the zinc-reinforced area than in the non-reinforced one. However, since the values for the non-reinforced cuticle are very close to those of the resin, additional tests need to be conducted on similar samples to verify the reliability of the results.

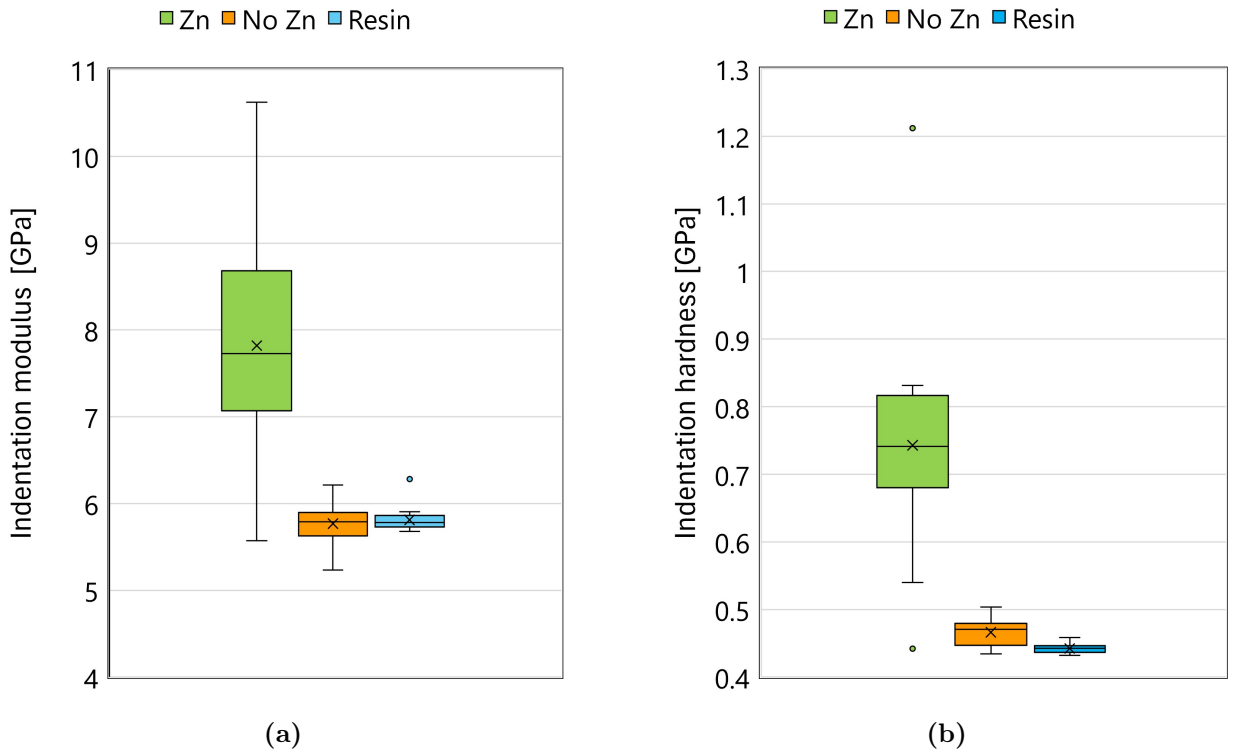

(a) **(b)**

Figure 44: Boxplots of indentation modulus and indentation hardness obtained from quasi-static nanoindentation on two different area of an *Acromyrmex octospinosus* minor mandible. The variability is very high in the zinc-reinforced area and the values obtained in the non reinforced area are very close to the ones obtained for the resin.

Formica rufa big (E)

The inner surface of this sample was uneven, so only a region near the surface was analyzed to assess its mechanical properties through quasi-static nanoindentation. The topography of this region is shown in the clickscript presented in Figure 45b

The main challenge with this data is the difficulty in recognizing the test area, complicating the correlation with mechanical properties. To obtain more reliable information, additional samples from this caste of *Formica rufa* ants should be tested.

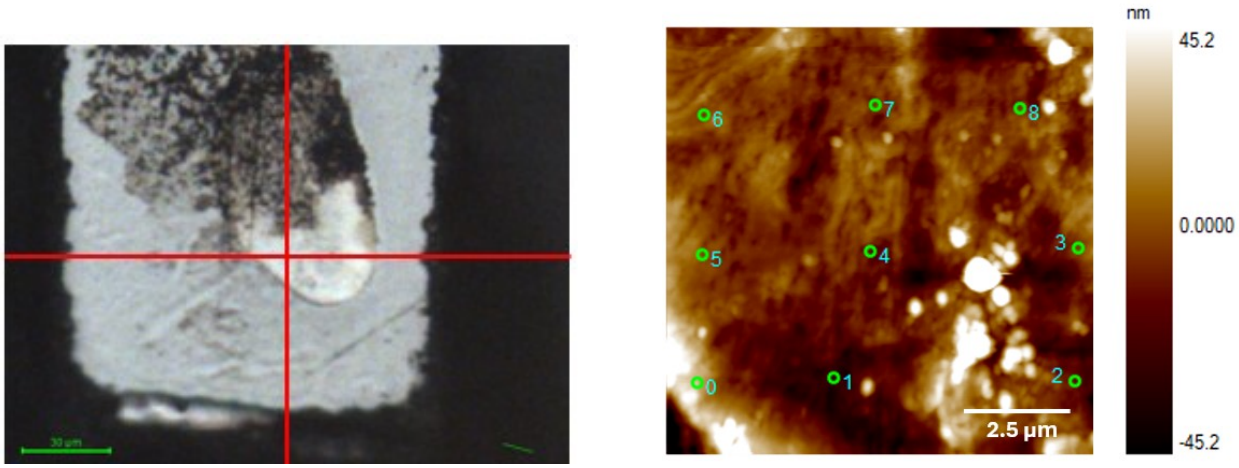

(a) **(b)**

Figure 45: Indications on the indented area: optical image in Figure 45a where the surface defects are visible and the tested area is indicated by the intersection of the two red lines. clickscript in Figure 45b.

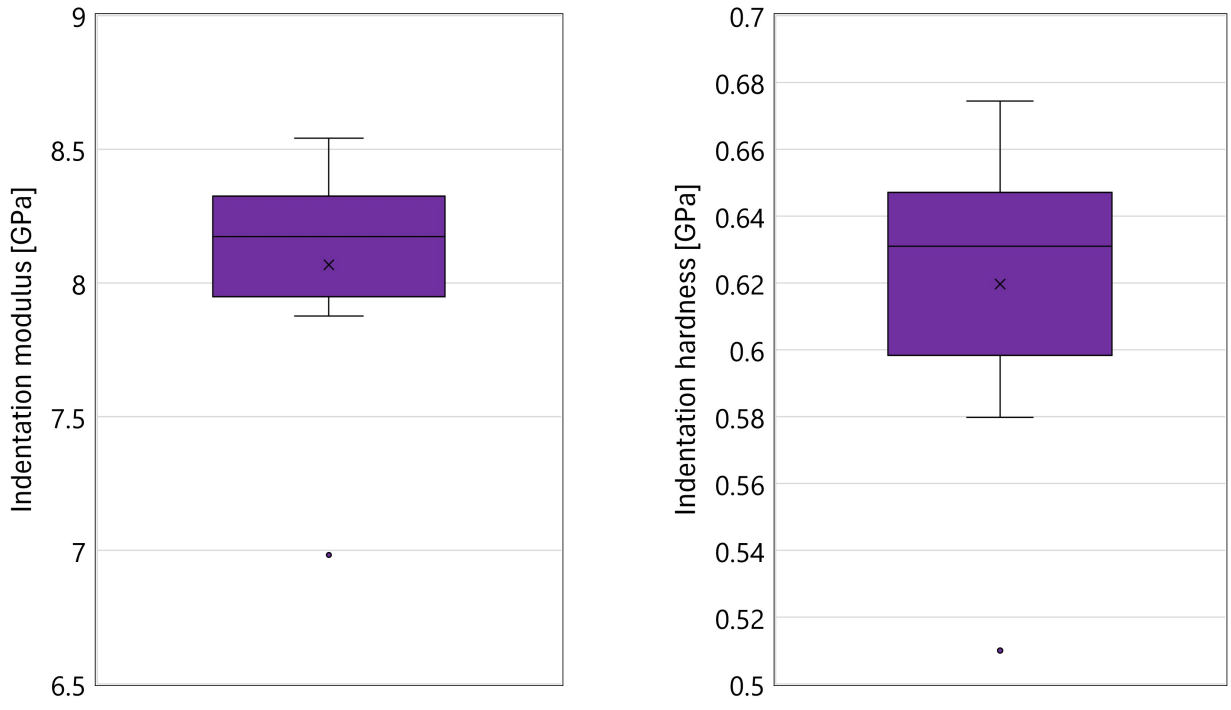

(a) **(b)**

Figure 46: Boxplots of indentation modulus and indentation hardness obtained from quasi-static nanoindentation. The average modulus of this area is slightly higher than the one of the reinforced area of *Acromyrmex octospinosus* major and hardness values are slightly lower, so this could be considered the harder area of the mandible.

Formica rufa small (G)

For this sample, elastic properties were measured in two distinct regions: one near the surface and one in the inner area of the mandible. These two areas where the properties were measured can be observed in Figure 47.

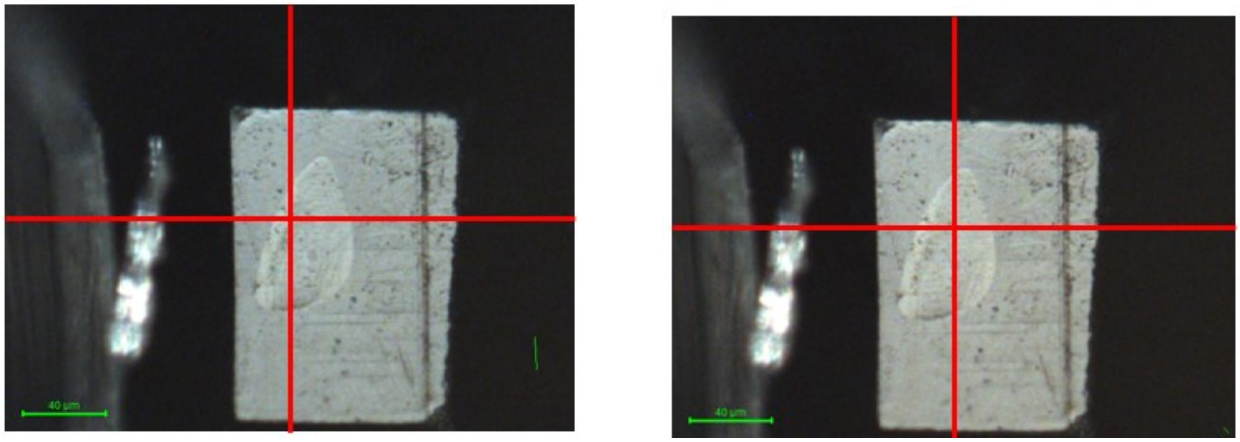

(a) **(b)**

Figure 47: Optical images of outer (47a) and inner (47b areas of sample G, the indented areas correspond to the ones indicated by the intersection of the lines.

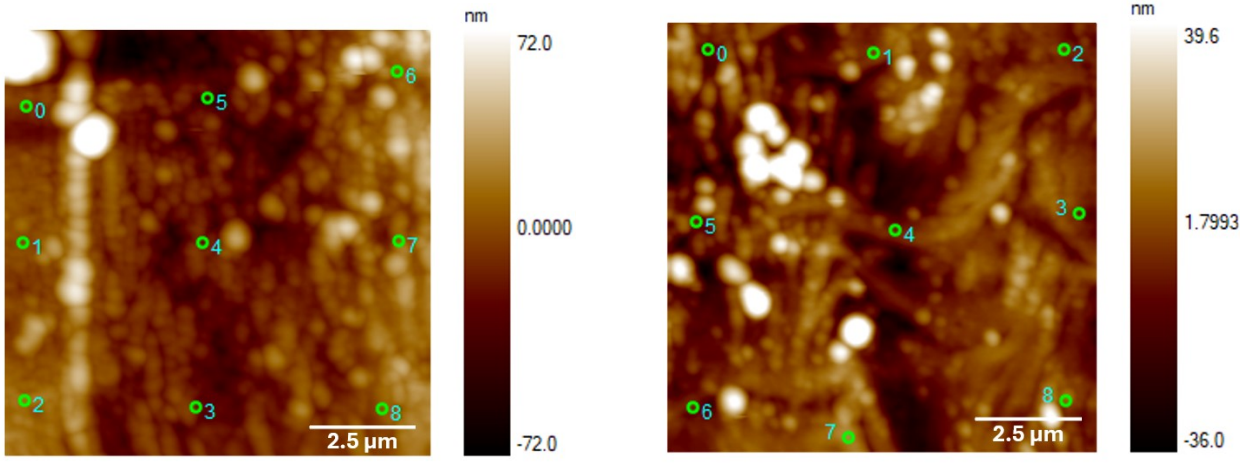

(a) **(b)**

Figure 48: Clickscripts of the indented areas on topographical images obtained with SPM. Outer (or surface) area in Figure 48a and inner (or inside) area in Figure 48b.

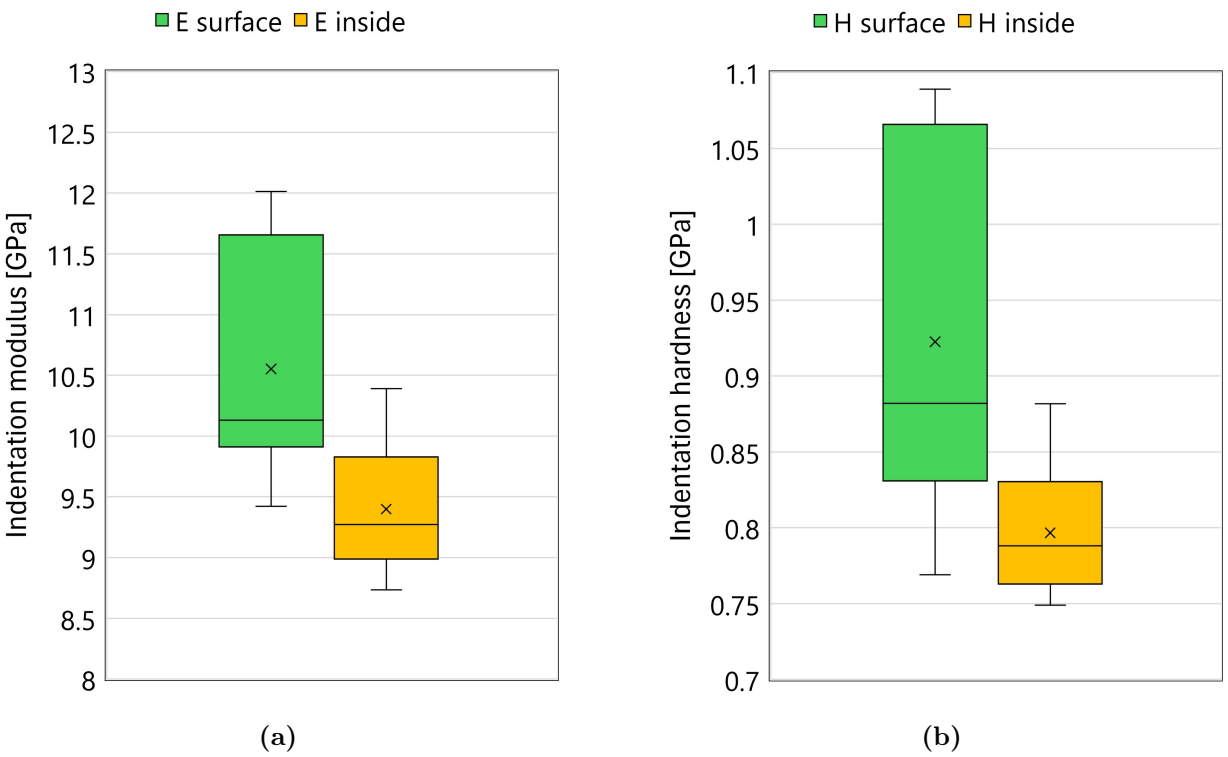

Figure 49: Boxplots of indentation modulus and indentation hardness on two different area of a *Formica rufa* minor mandible. The values of the outer area are very high even if they do not reach the ones measured in *Acromyrmex octospinosus*.

The properties of this sample were further mapped by conducting 100 equally spaced indentations (spacing of 3 μm between indents) within a 30 μm square area. The results are displayed in Figure 51, with the tested area shown in Figure 50.

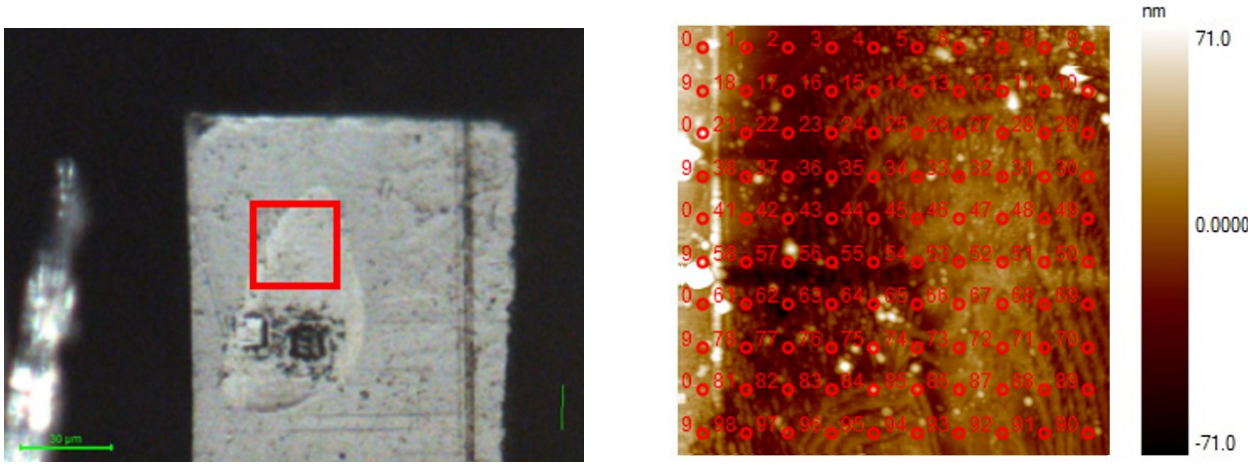

(a) (b)

Figure 50: In Figure 50a an optical image of the sample G with the indentation area indicated by a red square measuring 30x30 μm. In Figure 50b the location of the indents used for the 2D mapping of the the elastic properties, the side of the square measures 30 μm.

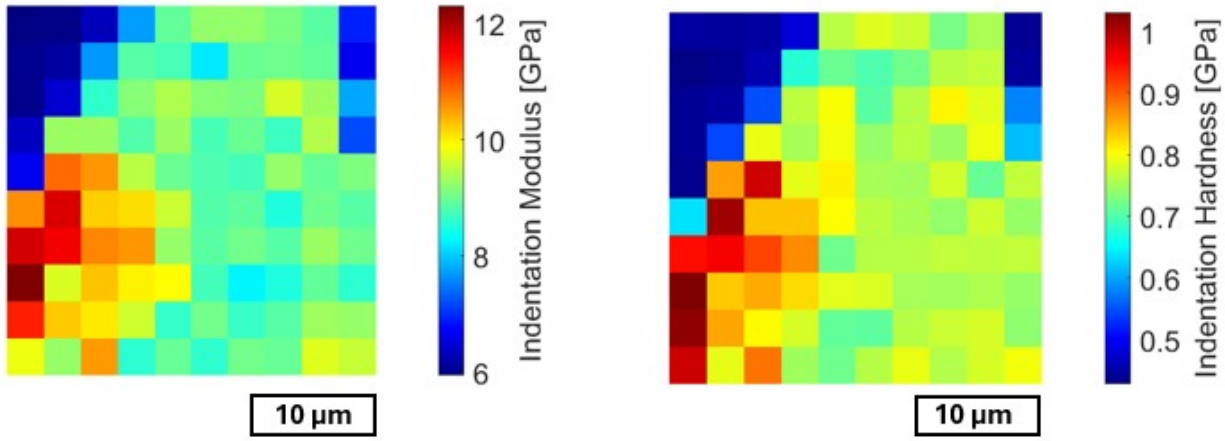

(a) (b)

Figure 51: 2D maps of indentation modulus (Figure 51a) and indentation hardness (Figure 51b). One area with particularly high properties is evident in both figures.

3.3.2 Stress Strain Nanoindentation

Stress-strain nanoindentation tests were performed on both the zinc-reinforced area and the non-reinforced cuticle of the *Acromyrmex octospinosus* major worker mandible (sample D4). In this section, the results presented were obtained using the load function illustrated in Figure 7 in Open Loop mode, with a probe tip radius of 5 μm. Results obtained with different parameters are presented in Appendix B.

The figures are arranged to facilitate visual comparison between the reinforced and non-

reinforced cuticle regions: figures related to the zinc-reinforced area are presented on the left, while those corresponding to the non-reinforced region are displayed on the right.

Figure 52 displays the the nanoindentation areas. A noticeable difference in the surface appearance of the two areas is already evident from these images. This difference is confirmed by the SPM images visible in Figure 53, where the positions selected for the indents are marked.

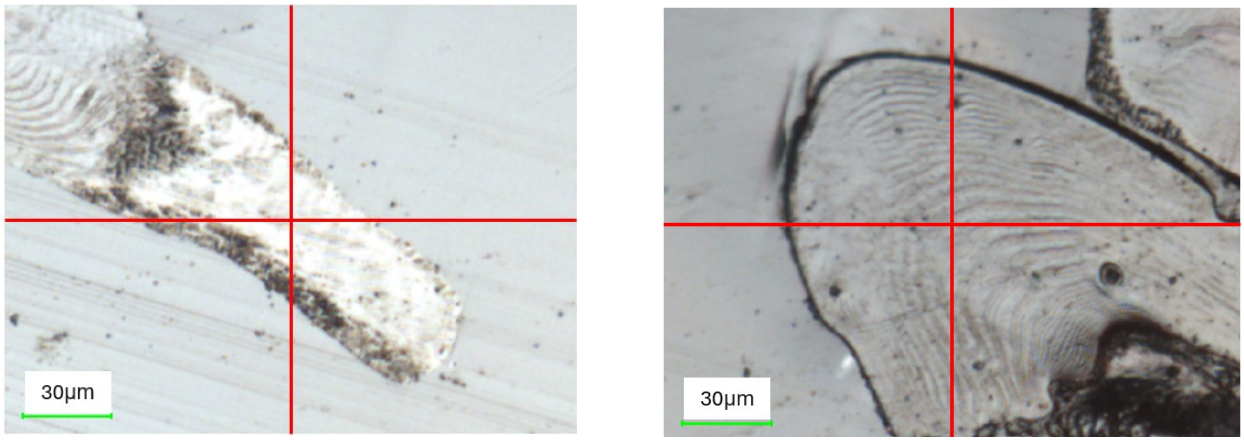

(a) **(b)**

Figure 52: Optical images of the nanoindentation areas in the zinc-reinforced (Figure 52a) and in the non-reinforced (Figure 52b) parts of the mandible.

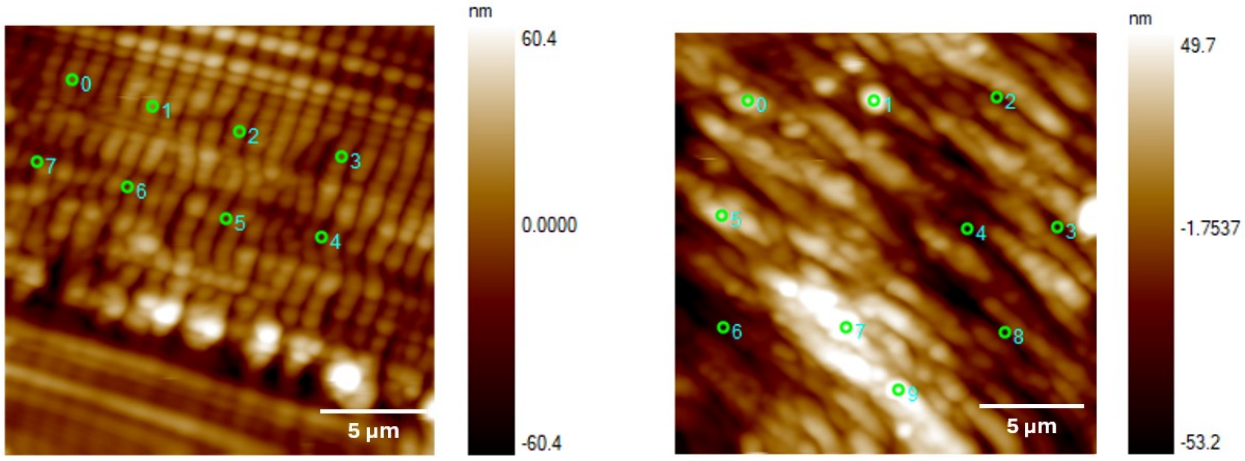

(a) **(b)**

Figure 53: Indent locations for the tests on the zinc-reinforced (Figure 53a) and in the non-reinforced (Figure 53b) parts of the mandible.

For each indent location, a stress-strain curve was plotted. All these curves are shown in the graphs in Figure 54. The curves corresponding to the indents in the zinc-reinforced area generally exhibit a steeper slope compared to those related to the non-reinforced area, indicating

lower deformation at equivalent stress levels. However, there are exceptions that highlight the complexity of the material, suggesting that it cannot be considered as homogeneous.

To better observe the nature of the deformation, one representative curve from each area was selected: indent 5 for the zinc-reinforced area and indent 2 for the non-reinforced area. These curves are plotted in separate graphs in Figure 55 for clearer visualization. Additionally, these stress-strain curves are correlated with the corresponding load-displacement curves, displayed in Figure 56, which provide additional informations regarding deformation behavior. Specifically, it can be observed that after reaching a certain load, the displacement does not return to zero when the probe of the nanoindenter is removed. This indicates that the deformation is no longer purely elastic. From these graphs, it is evident that this transition load is higher for the zinc-reinforced area.

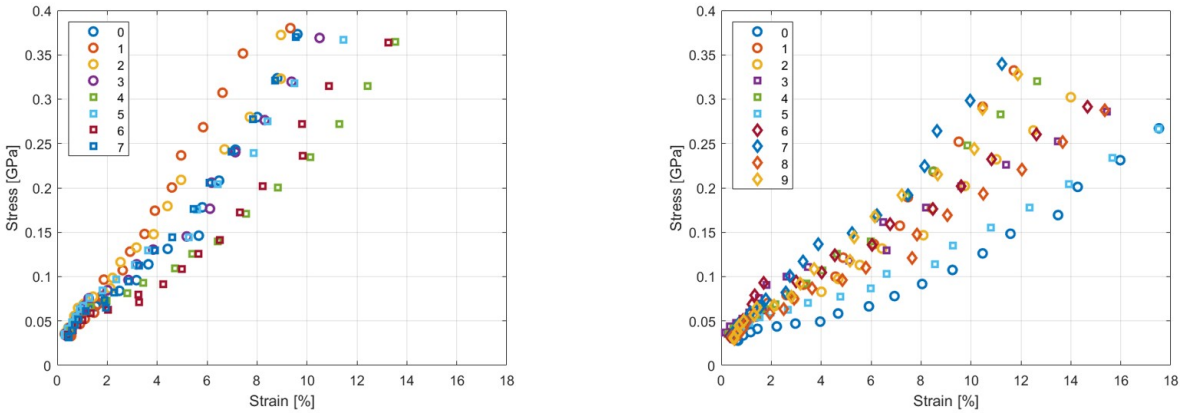

(a) **(b)**

Figure 54: Stress-strain curves relative to the indents performed in the zinc-reinforced area of the mandible (Figure 54a) and to the ones performed in the non-reinforced areas of the mandible (Figure 54b).

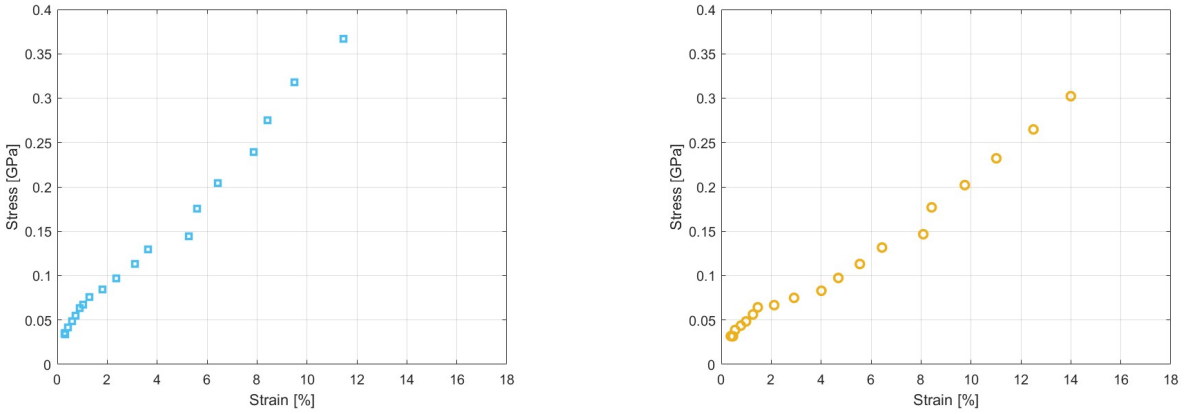

(a) **(b)**

Figure 55: Representative stress-strain curves for the zinc-reinforced (Figure 55a) and non-reinforced (Figure 55b) areas of the sample. Both curves have a linear part up until around 2% strain and then the slope changes, the slope variation is more pronounced in the non-reinforced cuticle.

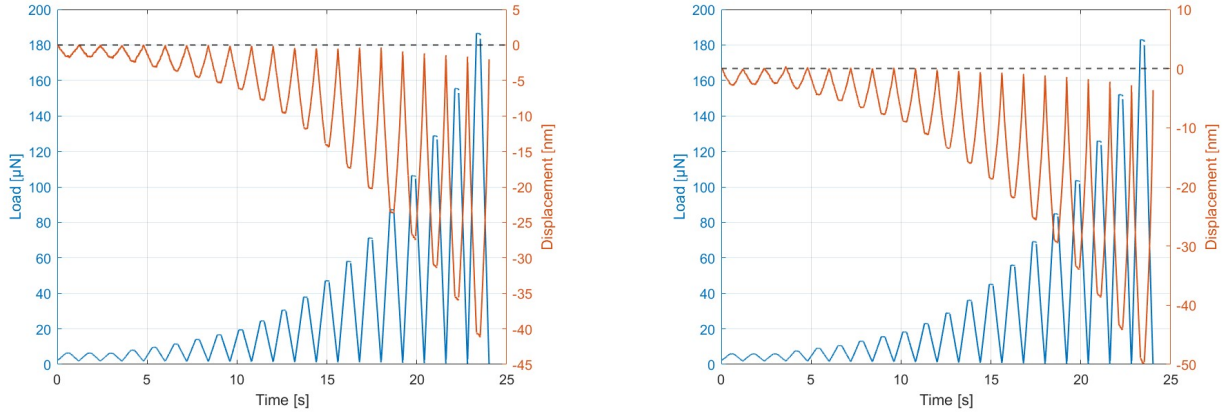

(a) **(b)**

Figure 56: Load-displacement curves relative to indent 5 in the zinc-reinforced area of the mandible (Figure 56a) and to indent 2 in the non-reinforced area of the mandible (Figure 56b). The behavior of the sample deviates from elasticity at lower displacements for the non-reinforced area.

3.3.3 Wear test

In this section, we report the results of the wear tests conducted on the four different samples. The comparisons follow the same structure as those in the quasi-static nanoindentation section. The primary quantitative result considered is the difference between the mean height of the intact area and the mean height of the area after the test, referred to as "wear height". While the "wear volume" could be obtained by multiplying the wear height by the tested area, this approach is complicated by the limited and varying areas available for some tests. Therefore, using "wear height" as the parameter facilitates easier comparison of results.

Acromyrmex octospinosus major (D4)

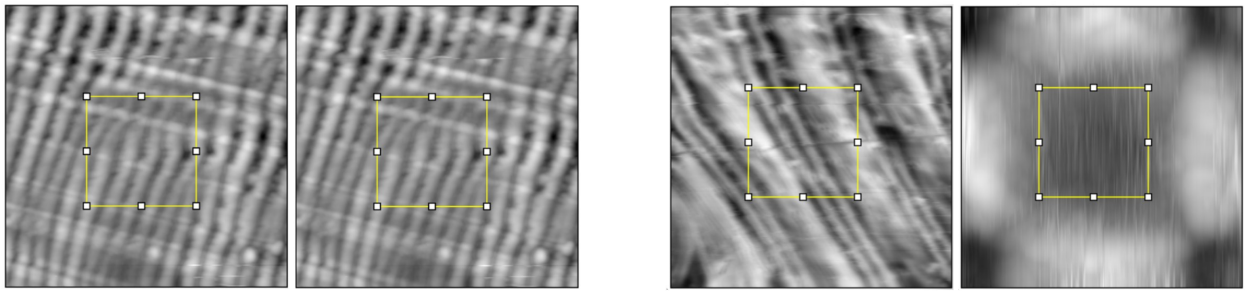

(a) **(b)**

Figure 57: Wear test on sample D4, zinc-reinforced area in Figure 57a and non-reinforced area in Figure **??**. The mean height considered in the results is the one inside the yellow squares.

Acromyrmex octospinosus minor (C3)

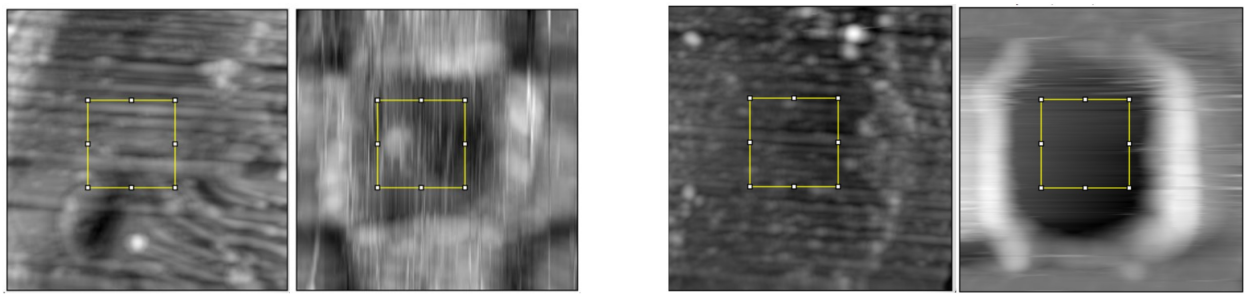

(a) **(b)**

Figure 58: Wear test on sample C3, zinc-reinforced area in Figure 58a and non-reinforced area in Figure 58b. The mean height considered in the results is the one inside the yellow square.

Formica rufa big (E)

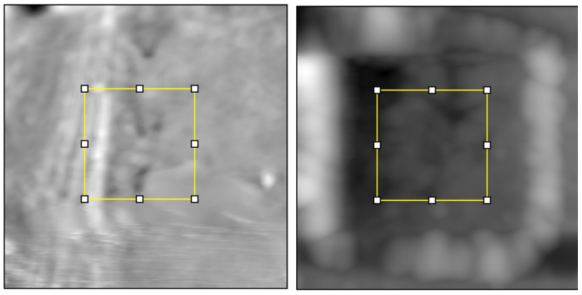

Figure 59: Wear test on sample E, the mean height considered in the results is the one inside the yellow square.

Formica rufa small (G)

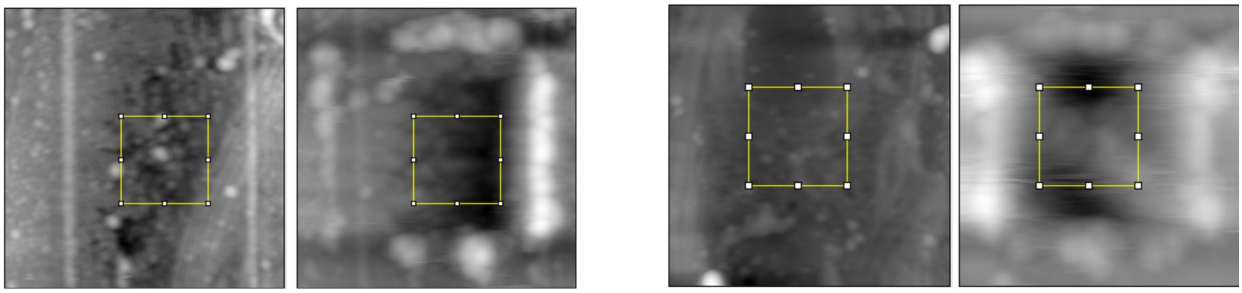

(a) **(b)**

Figure 60: Wear test on sample G, on the outer side of the sample in Figure 60a and on the inner side of the sample in Figure 60b. The mean height considered in the results is the one inside the yellow square.

In Table 5, the numerical results of the tests conducted with a force of 300 μN and ten passes of the different samples are reported.

Sample	Reinforced area	Non reinforced area
D4	1.091 nm	251.712 nm
C3	54.19 nm	212.713 nm
E	47.072 nm	non tested
G	95.293 nm	279.918

Table 5: Wear heights for all the tested samples.

From the results obtained from these tests, it is evident that the reinforced areas are clearly more wear-resistant than the non-reinforced ones. The reinforced areas in the major caste exhibit greater wear resistance compared to those in the minors ants, across both species. The most interesting result being the almost nonexistent effect of the wear test on *Acromyrmex octospinosus* major ant sample, this is a clear result of the wear resistance that the mandibles of this caste of ants have in order to be able to perform their function.

Different loads on Acromyrmex octospinosus major (D4) reinforced area

Motivated by the low wear height of the sample D4 when the wear test was conducted at a force of 300 μN, two additional tests were conducted on this sample: both of them with 10 SPM passes but the first with a load of 500 μN and the second with a load of 700 μN. These two tests were performed with the aim to observe the effect of increasing loads on wear resistance and to confirm the reliability of the previous experiment results.

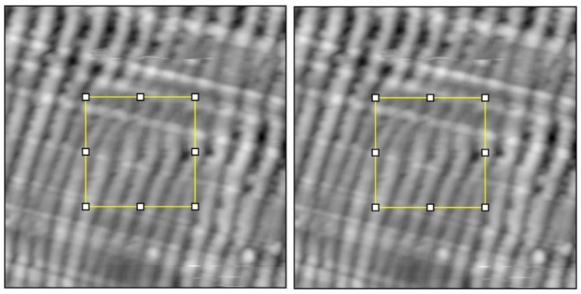

Figure 61: Topographic image before and after wear test at 300 μN.

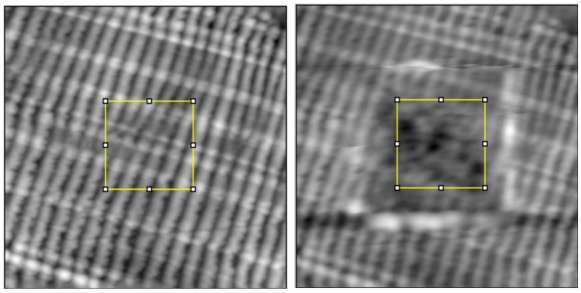

Figure 62: Topographic image before and after wear test at 500 μN.

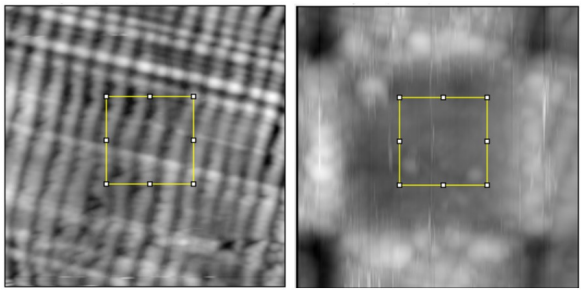

Figure 63: Topographic image before and after wear test at 700 μN.

From the results reported in Table 6, we see that the test that we conducted were reliable, since the wear height increases when increasing the load. Overall the high wear resistance of this area is noteworthy, at 700 μN the wear height of the area is comparable to that of other samples reinforced areas tested at 300 μN, This remarkable result could serve as a motivation for more in-depth research on this type of ant to elucidate the mechanisms responsible for such high wear resistance.

300 μN	**500 μN**	**700 μN**
1.091 nm	19.174 nm	55.85 nm

Table 6: Wear heights for zinc-reinforced area of sample D4 tested with increasing wear loads.

4. Discussion

The purpose of this section is to discuss the observations from the results section and relate them to the existing literature on similar topics. After this discussion, the main limitations encountered during the work are presented, followed by ideas that may be useful for continuing research on the same topic.

4.1 Morphology

Digital microscopy and X-ray micro-computed tomography enabled a detailed examination of the morphology of the heads and mandibles of two workers castes of *Acromyrmex octospinosus*: majors and minors. Several differences were observed between the two castes in terms of mandibles dimensions, shape and color: this differentiation of the workers subcastes reflects their distinct functional roles. A study by Klunk et al. on the mandible morphology of *Pheidole* ants, a genus of ants which exhibit dimorphic worker castes (majors and minors), utilized finite element analysis to simulate several load scenarios to which the mandibles of polymorphic workers could be subjected, to investigate the correlation between morphological variation between worker castes and bite loading demand [25].

In our study, although our observations are based on microCT and microscopy rather than finite element analysis, the clear specialization of *Acromyrmex octospinosus* workers, where the major caste is specialized for cutting fresh leaves and transport them to the nest, while the minors take care of the symbiotic fungus, suggests a link between the morphological traits of their mandibles and the specific mechanical demands of their tasks.

4.2 Metal distribution

The distribution of zinc in the mandibles was investigated using EDS spectroscopy. Consistent with findings in other animal tools, zinc was abundant in the areas of contact with the external environment (plant material for major workers, fungus for minors), likely enhancing hardness and wear resistance in these regions. Similar studies have demonstrated the significance of zinc in enhancing mechanical properties in selected areas where high performances are needed. For instance, Politi et al. observed selective incorporation of zinc in the fangs of the wandering spider *Cupiennius salei*, which contributes to the fang's ability to puncture insect cuticle [4]. Broomell et al. observed a uniform distribution of zinc in the section of the jaw of *Nereis virens* that was subjected to the highest stresses[3]. Johnston et al. have found that the zinc rich layers in the mandibles of *Atta cephalotes* directly correlated with increased hardness in the areas that come in contact with the leaves [18].

4.3 Mechanical properties

We conducted several tests to assess the mechanical properties of our samples, from the more classic nanoindentation to stress-strain analysis, concluding the analysis with wear tests. It is

quite easy to find numerical values to make comparison for standard measurements such as elastic modulus and indentation hardness, but it is quite challenging to find similar studies including stress-strain analysis and wear tests on comparable materials.

When we focus on the analysis of our results, it is important to notice that we used the data we obtained from single samples and that, due to their biological nature, samples present a high degree of variability related to many parameters that should be as controlled as possible in order to obtain reliable results.

4.3.1 Quasi-static nanoindentation

The results obtained from quasi-static nanoindentation such as indentation modulus and indentation hardness show that the elastic modulus and hardness are generally higher on the outer surface compared to the inner surface. This trend is observed both in zinc-reinforced mandibles, such as those of *Acromyrmex octospinosus* workers, and in mandibles hardened without the presence of transition metals such as the ones of *Formica rufa*. We also observed that the major workers mandibles have higher mechanical properties with respect to the minor ones, evidencing the different mechanical demands required by their specific role in the colony work.

Cribb et al. [19] conducted a comparative analysis of the mean hardness and mean reduced modulus across six termite species, including samples with high zinc concentrations, minor manganese, and no metals. Their findings demonstrated that mandibles of fully developed individuals lacking metals exhibit lower hardness and elastic modulus values. Our tests on *Formica rufa* were inspired by this comparative approach between different species.

We observed the highest mechanical properties for the zinc-reinforced area of the mandible of *Acromyrmex octospinosus* majors while the only tested sample of minor exhibited relatively low mechanical properties. The number of samples tested for majors can be considered satisfactory, since we also conducted some on two polished samples (Appendix D) that led to comparable results, but a higher number of experiments should be performed both on *Formica rufa*, and on fully developed individuals of *Acromyrmex octospinosus* minors. The age of the samples could be particularly significant since Schofield et al. demonstrated that the hardness of the mandibular tooth in *Atta sexdens* increases nearly three-fold as the adults age, and that hardness correlates with zinc content [5].

In a study by Schofield et al. [2] various mechanical properties were examined across a range of zinc-reinforced animal tools. The results showed that the mean hardness in the zinc-reinforced areas ranges from 0.78 to 1.41 GPa, with an elastic modulus between 9.2 and 16 GPa. Our experimental values align with these results, indicating coherence with the literature on similar reinforced tools.

4.3.2 Stress-strain analysis

Indentation stress-strain curves with micrometre spatial resolution to study the deformation behavior of biological material have been used by Amini et al. [15] to investigate the role

of quasi-plasticity in the contact damage tolerance of the stomatopod dactyl club. The key mechanical properties of the subject of our study are hardness, stiffness and wear resistance, which are more closely associated with the elastic portion of deformation.

In our study, the stress-strain curves for both reinforced and non-reinforced areas of the mandible of the major worker exhibit an initial linear region between 0 and 2% strain, beyond this point the slope strongly decreases in the non reinforced area , while in the curves related to the zinc-reinforced region the decrease is less pronounced. The values of stress imposed are significantly lower compared to the ones in the article by Amini, where a yield point is found in the stress-strain curves [15].

As long as we know this kind of analysis has never been conducted before on leafcutter ants mandibles and the curves obtained from our tests are not straightforward to interpret.

4.3.3 Wear resistance

The methodology of the wear tests we conducted was inspired by the one followed by Pontin et al. in their study about abrasion resistance in the jaws of *Glycera dibranchiata*, an animal tool that is reinforced with copper [1]. Pontin's research identified distinct microstructural domains within the jaws, the unmineralized copper reinforced domains exhibited the highest abrasion resistance.

Our tests focused on two different regions of the mandible, the one close to the teeth that is reinforced with zinc, and the cuticle on the other side of the mandible, that we often called "non-reinforced" throughout this work. From our tests we concluded that the zinc reinforced areas possess superior wear resistance, a finding that aligns with Pontin's conclusions, despite the different biological subjects and the different metal used for reinforcement [1].

The consistency between these results suggests that the presence of certain microstructural features, such as unmineralized metals, plays a critical role in enhancing wear resistance across different biological materials.

The most interesting result obtained from the wear tests we performed is the superior wear resistance of the zinc reinforced area of *Acromyrmex octospinosus* major workers mandibles, compared to that of other tested samples. This result motivated us to conduct various tests on this type of samples, all of them confirmed the initial findings.

Wear resistance is one of the most important mechanical properties for mandibles the major workers leafcutter ants, since worn out mandibles increase the energy consumed by the ants to cut leaves.

4.4 Limitations

During this study we encountered some limitations, which are discussed in this section with the aim to help future research on this topic.

One of the most significant limitations was the use of only one sample per type of ant. This amount of samples is not sufficient for performing a statistically relevant analysis, as biological

samples naturally exhibit variability. The lack of multiple samples for each ant type restricts the ability to draw definitive conclusions and increases the potential for anomalous results. For future studies, it is important to use a larger number of samples per ant type to account for biological variability and improve the reliability and statistical significance of the findings.

Another limitation was the absence of a standardized protocol in the literature for testing arthropods cuticle. The cuticle is a complex structure, and variations in testing methods can lead to inconsistent results. Without a standardized procedure, it is challenging to compare results across different studies or to replicate findings accurately. The development and adoption of a standard testing protocol would enhance the consistency and comparability of future research in this field, which is important to build foundations to understand the mechanical properties of cuticle and of metal reinforcement in animals tools.

It is also worth noting that the *Formica rufa* samples used in this study were prepared previously. The conditions under which these samples were stored and handled before testing could have influenced their mechanical properties, potentially introducing additional variability into the results. Future research should consider the impact of sample storage and handling on the outcomes, and where possible, aim to use freshly prepared samples to minimize potential sources of error.

Finally, the issue of detachment between the resin and the cuticle posed a significant challenge. Being the cuticle highly impermeable it is difficult to find a way to increase the adhesion between cuticle and the medium in which the sample is embedded, but the detachment between the two could affect the measured values for mechanical properties of the sample: when the cuticle is not sufficiently adherent to the resin in which it is embedded, the sample may move during testing, leading to inaccurate measurements. Finding a way to avoid any possible movement of the samples during mechanical testing is a crucial challenge for future research on this topic.

4.5 Future works

A promising direction for future research is to use confocal microscopy on rhodamine-stained samples to observe the internal structure of the mandibles. In this study, two samples of major workers were successfully stained with rhodamine, which penetrated their mandibles effectively, indicating the potential of this technique for further analysis.

Additionally, using scanning electron microscopy to examine the nanoindented samples could provide valuable insights. This approach would allow for the observation of wear marks left by mechanical tests, helping to understand how material removal varies across different areas of the mandibles.

Comparative studies across different worker castes could also be valuable. Testing media workers could provide further insights, but to gain a comprehensive understanding, it is essential to develop effective methods for handling and preparing samples from the minor caste, despite their significantly smaller size

The next steps should focus on optimizing and standardizing sample preparation and testing protocols, as well as increasing the number of samples analyzed to ensure more reliable results.

5. Conclusions

The primary objective of this thesis was to provide a comprehensive analysis of the zinc-reinforced mandibles of *Acromyrmex octospinosus* majors and minors workers, focusing on their morphology, composition, and mechanical properties. Based on the results obtained with the characterization techniques employed in this study, the following conclusions have been drawn:

- The most noticeable morphological difference between the minors and the majors is the size. Both castes have curved mandibles, with initial observations suggesting that the teeth of the minors may be sharper. However, this perceived sharpness could be influenced by factors such as the age of the ants.
- Zinc is present in the mandibles of the two analyzed *Acromyrmex octospinosus* workers castes, it is concentrated along the teeth, where the mandibles make contact with external environment, which can be both leaves of fungus in the nest. Zinc-reinforced and non-reinforced areas are clearly separate, with no evidence of a gradient in zinc concentration.
- The zinc-reinforced regions of the mandibles in both worker castes are significantly stiffer, harder, and more resistant to wear compared to the non-reinforced areas.
- The mandibles of major workers are notably harder and stiffer than those of minors, reflecting the different roles these castes play within the ant colony.
- To ensure accurate comparisons between different samples, it is crucial to develop a standardized sample preparation protocol and increase the number of tested samples for each ant type.

6. Appendices

A. TEM and STEM

Thin slices of 70 nm, cut with a microtome, were observed using Transmission Electron Microscopy (TEM) to gather information about the structural organization of the fibrils near the tip of the mandibles. However, numerous technical difficulties were encountered, and most samples were not detectable during observation. The only observable sample was a thin slice from an *Acromyrmex octospinosus* minor sample, but interpreting the structural organization from these images proved challenging. Nevertheless the TEM and STEM images of this sample are presented in Figure 64 and showing features such as the detachment of the cuticle from the resin, the presence of some cells, and defects resulting from the microtome's cutting vibrations.

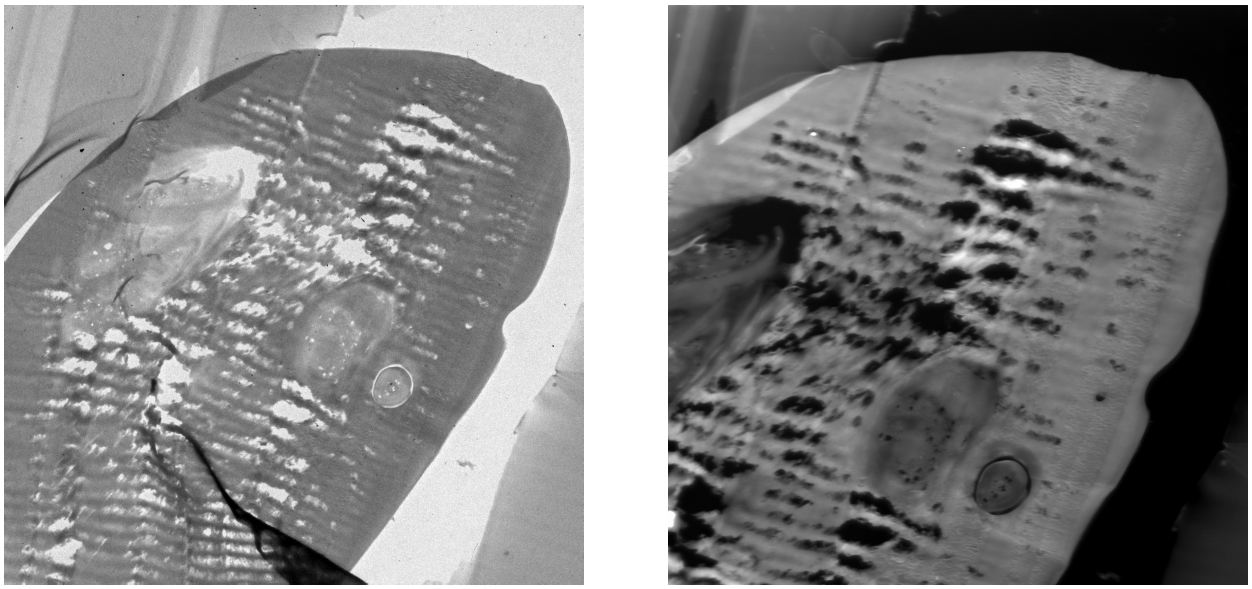

(a) **(b)**

Figure 64: Images of a slice of sample C3 produced with TEM (Figure 64a) and with STEM (Figure 64b).

B. Stress strain nanoindentation with preload

The result of the stress-strain nanoindentation experiments performed on sample D4 present significant variability, to evaluate the effect of surface roughness on those results we applied a preload of 20 μN before initiating the cyclic loading characteristic of the experiment. The preload application aim is to flatten the surface on the location to be indented and reduce the variability in roughness that could contribute to the results variability.

During this experiments however the load application mode was changed from open loop to load control, since by observing the load-displacement graphs for previous experiments we noticed that the load would not reach the selected value. The stress-strain curves obtained with these parameters are reported here. Since two variables were altered simultaneously, it is not possible to isolate the effect of the preload. Future experiments should repeat this technique while maintaining the Open Loop setting to determine if the preload contributes to the homogenization of the stress-strain curves.

In Figure 67 the stress-strain curves obtained under these conditions are presented for both the zinc-reinforced area and the non-reinforced area. To align with the structure used in the results section, optical images of the indented areas and their corresponding clickscripts are displayed side by side.

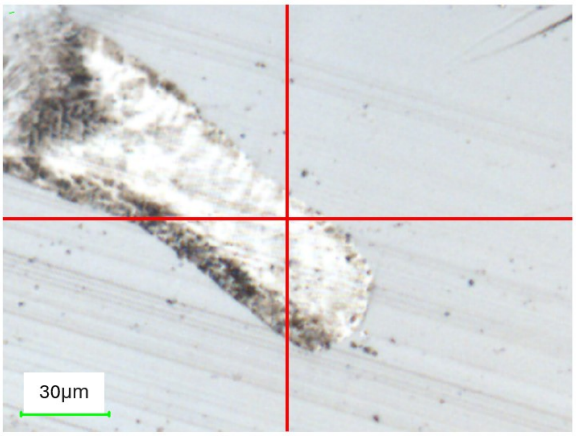

(a)

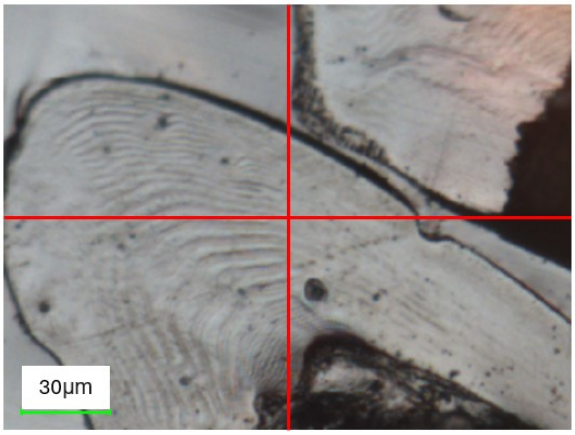

(b)

Figure 65: Optical images of nanoindentation area in the zinc reinforced part of the mandible (Figure 65a) and in the non-reinforced part of the mandible (Figure 65b).

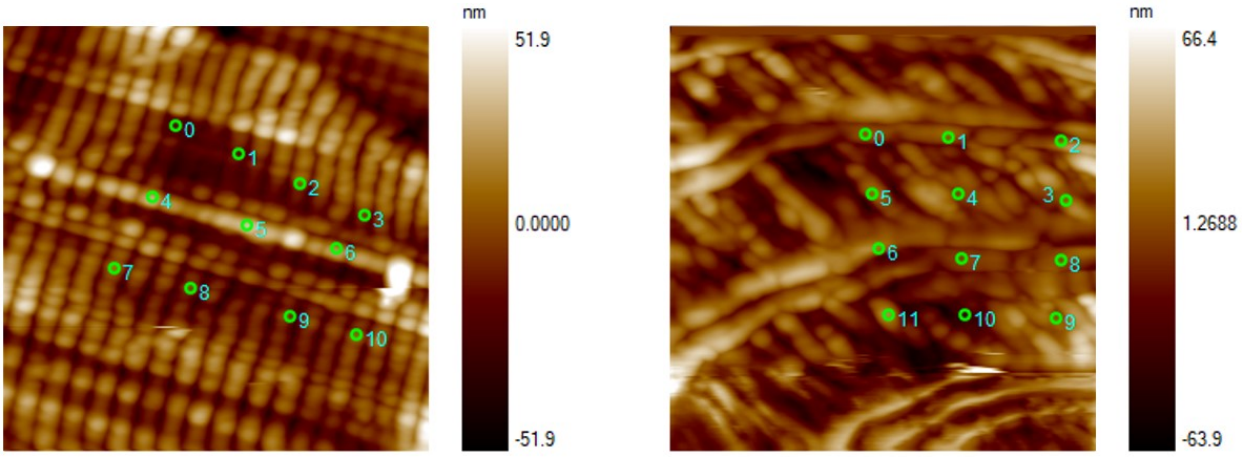

(a) **(b)**

Figure 66: Clickscripts reporting indent locations in the the zinc-reinforced area of the mandible (Figure 66a) and in the non-reinforced one (Figure 66b).

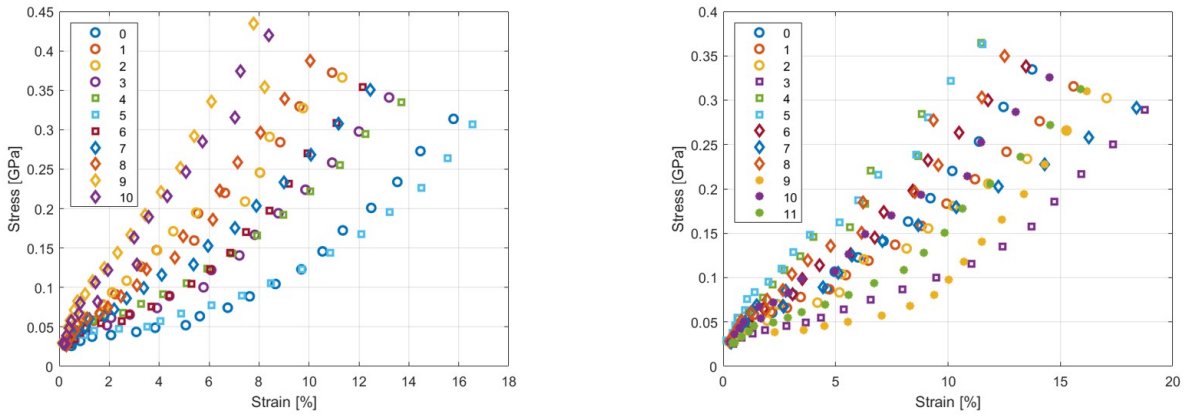

(a) **(b)**

Figure 67: Stress-strain curves relatives to the indents performed in the reinforced area of the mandible (Figure 67a and in the non-reinforced one (Figure 67b).

Taking into account that the loading mode changed, we can observe that with respect to the stress strain indentations performed without preload in the results section (Figures 54) there is no evidence of reduced variability between curves relative to different indents.

C. Stress strain nanoindentation in resin

We performed stress-strain nanoindentation in the epoxy resin, in which samples were embedded, using a preload of 20 μN and operating in Open Loop mode. The resulting stress-strain curves are provided in this appendix for reference.

The high homogeneity of these curves indicates the uniformity of the material. This consistency confirms that the variability observed in the stress-strain curves reported in Figures 54 and 67 is attributable to the material itself, rather than to the testing parameters or procedural errors.

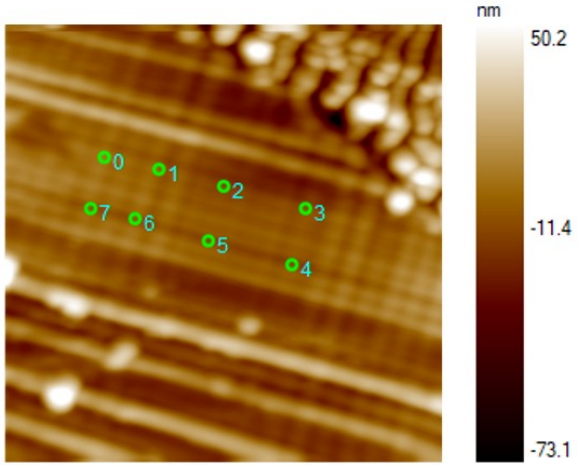

Figure 68: Clickscript indicating the locations of indents performed in resin.

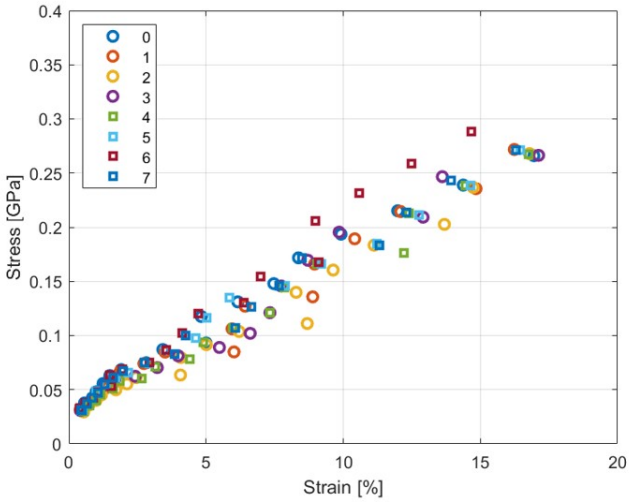

Figure 69: Stress-strain curves in resin. The low variability of the curves corresponds to an homogenous material.

D. Nanoindentation on polished samples

The results of nanoindentation experiments of samples prepared as indicated in Section 2.1.1 are reported in this appendix. The two samples that were polished are both of *Acromyrmex octospinosus* major workers and are called R1 and R2. The two samples were stained with rhodamine before polishing, this operation does not change the mechanical properties of the samples.

By comparing the SPM images of these samples, reported in Figures 70 and 72, to the ones of the samples prepared with the microtome (reported in the results section) it is evident that the samples prepared with this method are smoother, particularly the zinc-reinforced areas.

D.0.1 Quasi-static nanoindentation

Compared to the results obtained for sample D4 41, obtained with 9 indents, the variability of the values obtained for indentation modulus and indentation hardness is significantly reduced, even when 16 indents are performed (sample R2), this means that the preparation method actually has an effect on the result and polishing is a valid sample preparation method to measure the elastic properties of cuticle. The values obtained for sample R1 and R2 are different, confirming the variability of properties depending on samples.

Sample R1

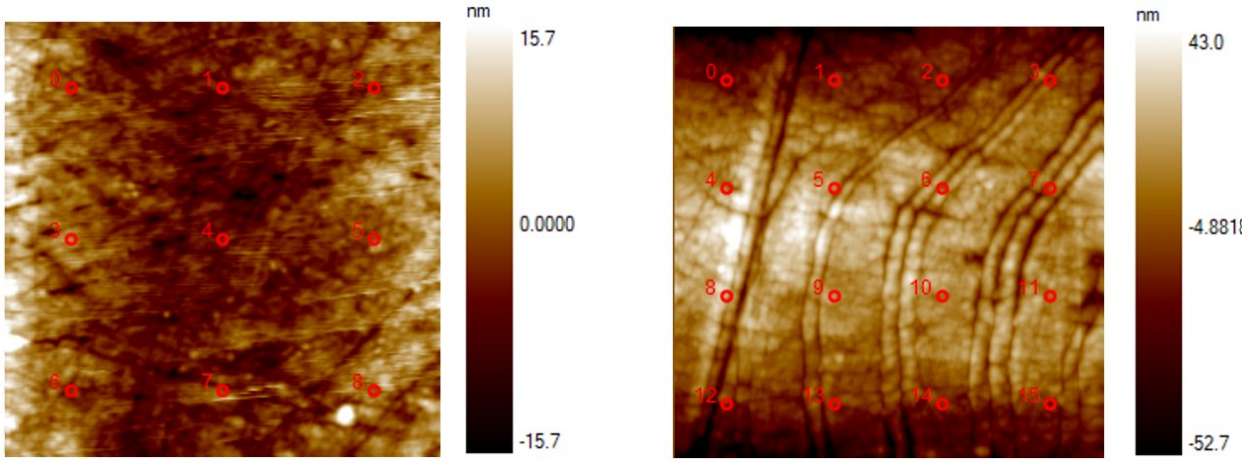

(a) **(b)**

Figure 70: Indentation locations for quasi-static experiments of sample R1 in zinc-reinforced area of the mandible (Figure 70a) and in non-reinforced one (Figure 70b).

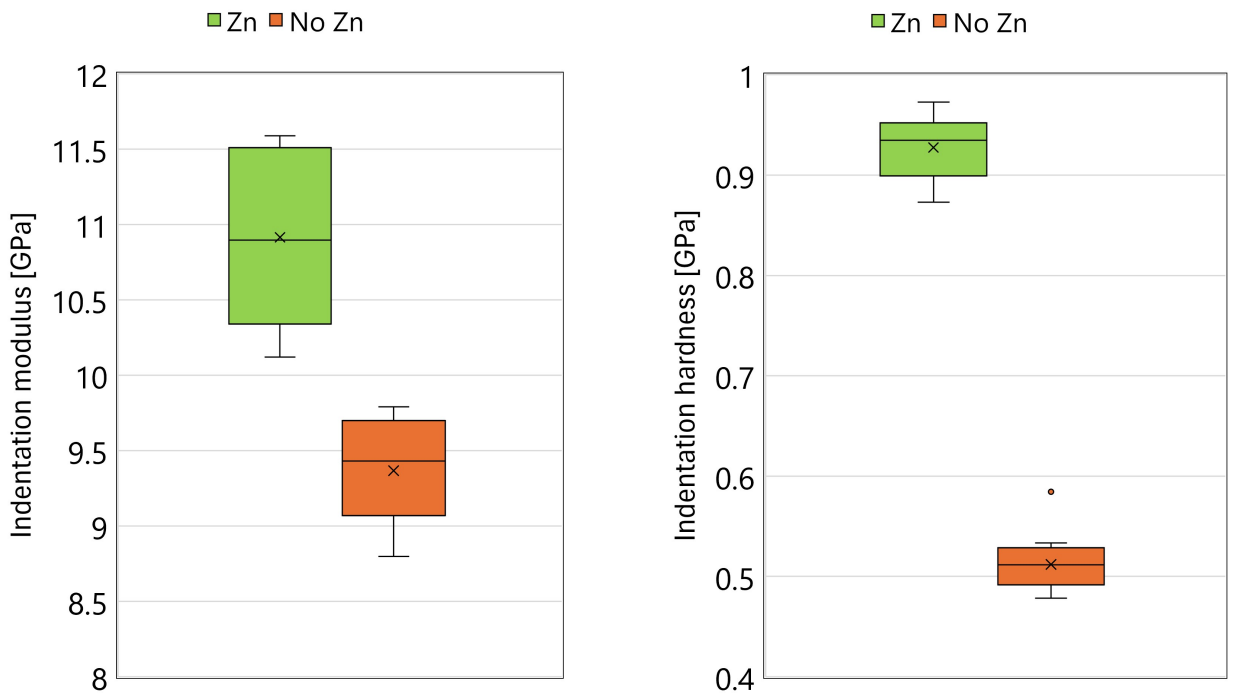

(a) **(b)**

Figure 71: Boxplots of reduced modulus (Figure 71a) and hardness (Figure 71b) obtained from quasi-static nanoindentation on two different areas of *Acromyrmex octospinosus* major workers mandibles polished sample R1.

Sample R2

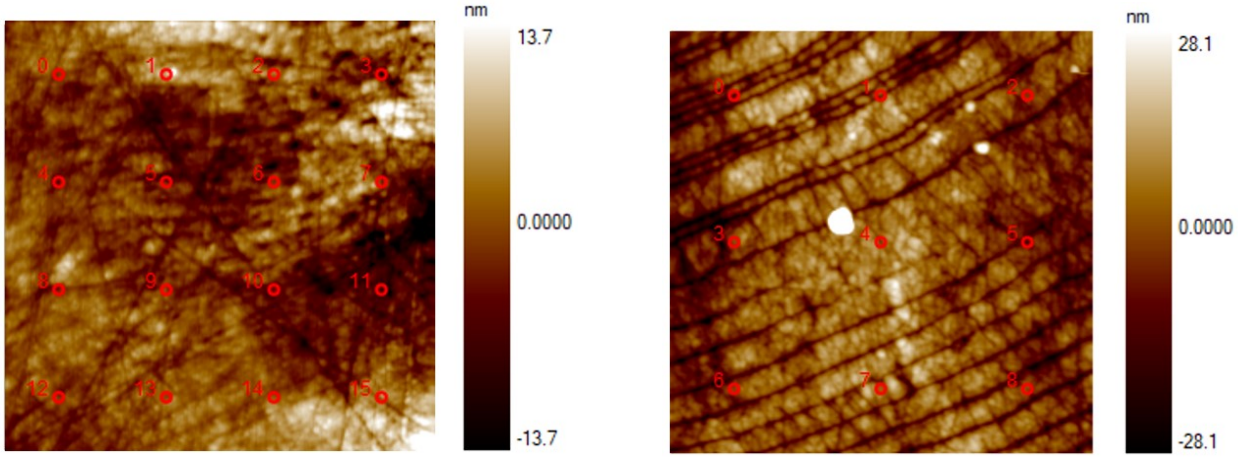

(a) **(b)**

Figure 72: Indentation locations for quasi-static experiments of sample R2 in zinc-reinforced area of the mandible (Figure 72a) and in non-reinforced one (Figure 72b).

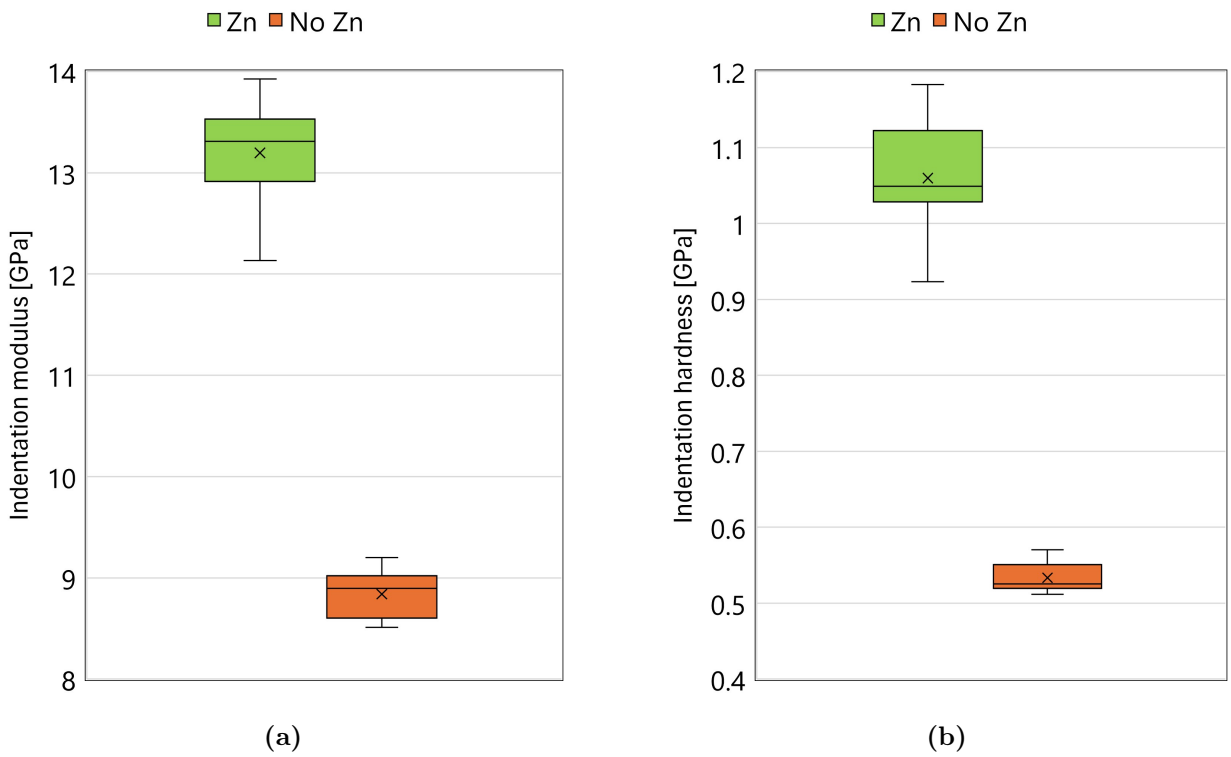

(a) **(b)**

Figure 73: Boxplots of reduced modulus (Figure 73a) and hardness (Figure 73b) obtained from quasi-static nanoindentation on two different areas of *Acromyrmex octospinosus* major workers mandibles polished sample R2.

D.0.2 Wear tests

The experiments conducted on these samples confirm the results of the ones conducted on the samples cut with the microtome, evidencing how the area reinforced with zinc in the major worker of *Acromyrmex octospinosus* is incredibly wear resistant. Sample R1, with measured elastic properties slightly inferior to the ones of sample R2 has also lower wear resistance, confirming the reliability of the experiments.

Sample R1

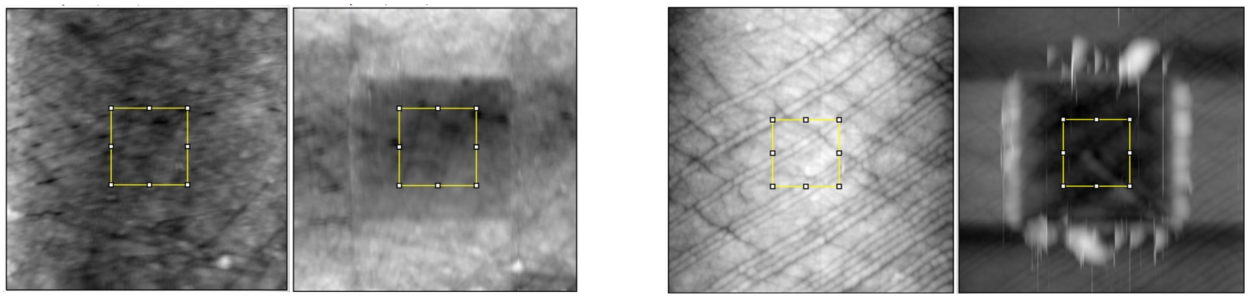

(a) **(b)**

Figure 74: Wear test on sample R1, in the zinc-reinforced area (Figure 74a) and in the non-reinforced one (Figure 74b) the mean height reported in the results is the one measured inside the yellow square.

Sample R2

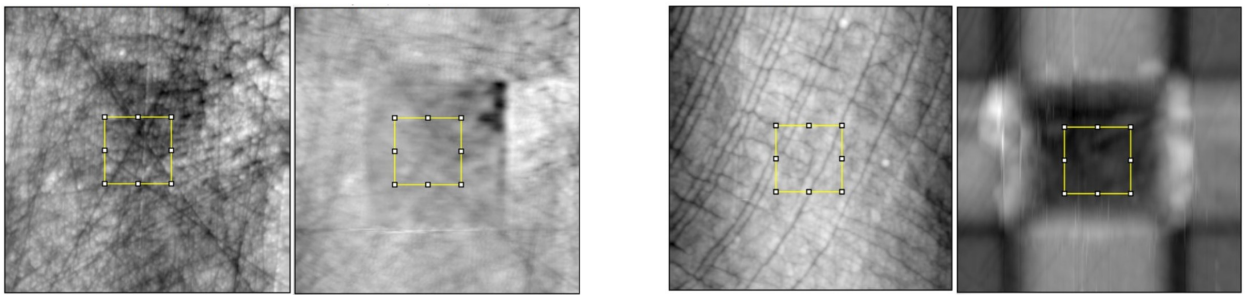

(a) **(b)**

Figure 75: Wear test on sample R2, in the zinc-reinforced area (Figure 75a) and in the non-reinforced one (Figure 75b, the mean height reported in the results is the one measured inside the yellow square.

Sample	Reinforced area	Non reinforced area
R1	8.845 nm	113.699 nm
R2	0.209 nm	156.68 nm

Table 7: Wear heights for the polished samples.

References

[1] J Herbert Waite Frank W Zok Michael G Pontin, Dana N Moses. A nonmineralized approach to abrasion-resistant biomaterials. *PNAS*, 2007.

[2] R. Schofield, J. Bailey, J. Coon, Arun Devaraj, R. Garrett, Matthew Goggans, M. Hebner, B. Lee, D. Lee, N. Lovern, Sidnee Ober-Singleton, N. Saephan, V. Seagal, D. Silver, Hishamuddin Som, J. Twitchell, X. Wang, J. Zima, and Michael Nesson. The homogenous alternative to biomineralization: Zn- and mn-rich materials enable sharp organismal "tools" that reduce force requirements. *Scientific Reports*, 11, 09 2021.

[3] Mike A. Mattoni Frank W. Zok Broomell, Chris C. and Herbert J. Waite. Critical role of zinc in hardening of nereis jaws. *Journal of experimental biology*, 209, 2006.

[4] Yael Politi, Matthias Priewasser, Eckhard Pippel, Paul Zaslansky, J. Hartmann, Stefan Siegel, Chenghao Li, Friedrich Barth, and Peter Fratzl. A spider's fang: How to design an injection needle using chitin-based composite material. *Advanced Functional Materials*, 22, 06 2012.

[5] Robert M. S. Schofield, Michael H. Nesson, and Kathleen A. Richardson. Tooth hardness increases with zinc-content in mandibles of young adult leaf-cutter ants. *Naturwissenschaften*, 89:579–583, 2002.

[6] John Dunlop Peter Fratzl Yuri Estrin, Yves Bréchet. *Architectured Materials in Nature and Engineering*. Springer Cham, 2019.

[7] J J Coon A Devaraj R W Garrett M S Goggans M G Hebner B S Lee D Lee N Lovern S Ober-Singleton N Saephan V R Seagal D M Silver H E Som J Twitchell X Wang J S Zima M H Nesson R M S Schofield, J Bailey. The homogenous alternative to biomineralization: Zn- and mn-rich materials enable sharp organismal "tools" that reduce force requirements. *Nature*, 2022.

[8] Isabelle Boulogne, Harry Ozier-Lafontaine, and Gladys Loranger-Merciris. *Leaf-Cutting Ants, Biology and Control*, volume 13, pages 1–17. 07 2014.

[9] Bruker MicroCT. *Skyscan 1172 User Manual*. Bruker Corporation, 2013.

[10] Eric N. Landis and Denis T. Keane. X-ray microtomography. *Materials Characterization*, 61(12):1305–1316, 2010.

[11] Yuchuan Liu, Dongyang Xie, Rifeng Zhou, and Yuxin Zhang. 3d x-ray micro-computed tomography imaging for the microarchitecture evaluation of porous metallic implants and scaffolds. *Micron*, 142:102994, 2021.

[12] Kalsoom Akhtar, Shahid Ali Khan, Sher Bahadar Khan, and Abdullah M. Asiri. *Scanning Electron Microscopy: Principle and Applications in Nanomaterials Characterization*, pages 113–145. Springer International Publishing, Cham, 2018.

[13] Ran He, Sonika Gahlawat, Chuanfei Guo, Shuo Chen, Tulashi Dahal, Hao Zhang, Weishu Liu, Qian Zhang, Eyob Chere, Kenneth White, and Zhifeng Ren. Studies on mechanical properties of thermoelectric materials by nanoindentation. *physica status solidi (a)*, 212(10):2191–2195, 2015.

[14] Warren C. Oliver and George M. Pharr. An improved technique for determining hardness and elastic modulus using load and displacement sensing indentation experiments. *Journal of Materials Research*, 7:1564–1583, 1992.

[15] Shahrouz Amini, Maryam Tadayon, Sridhar Idapalapati, and Ali Miserez. The role of quasi-plasticity in the extreme contact damage tolerance of the stomatopod dactyl club. *Nature materials*, 14(9):943–950, 2015.

[16] Li Hong He, Naoki Fujisawa, and Michael V. Swain. Elastic modulus and stress–strain response of human enamel by nano-indentation. *Biomaterials*, 27(24):4388–4398, 2006.

[17] Gaelle Sandront. Stress-strain characterisation of fibrolamellar bone. Master's thesis, University of Liège, 2023. Unpublished.

[18] Richard E Johnston, Mohammed Wakib Said, David Labonte, James Russell, Elizabeth Sackett, and Rachel Board. Correlative structure-property characterisation of the leaf-cutter ant (atta cepholotes) mandible. *Microscopy and Microanalysis*, 28(S1):1342–1346, 2022.

[19] Bronwen Cribb, Aaron Stewart, Han Huang, Rowan Truss, Barry Noller, Ronald Rasch, and Myron Zalucki. Insect mandibles-comparative mechanical properties and links with metal incorporation. *Die Naturwissenschaften*, 2007.

[20] Robert Schofield, Kristen Emmett, Jack Niedbala, and Michael Nesson. Leaf-cutter ants with worn mandibles cut half as fast, spend twice the energy, and tend to carry instead of cut. *Behavioral Ecology and Sociobiology*, 65:969–982, 05 2011.

[21] Helga C. Lichtenegger, Thomas Schö Berl, Janne Ruokolainen, Julie O. Cross, Steve M. Heald, Henrik Birkedal, J. Herbert Waite, Galen D. Stucky, and Kenneth N Raymond. Zinc and mechanical prowess in the jaws of nereis, a marine worm. *Proceedings of the National Academy of Sciences of the United States of America*, 100:9144 – 9149, 2003.

[22] Hysitron. *TI 980 TriboIndenter User Manual*. Hysitron Inc., 2016.

[23] Stephen Badger. In situ spm for nanomechanical and nanotribological characterisation, 2017. `https://blue-scientific.com/in-situ-spm-nanomechanical-nanotribological-characterisation/` [Accessed: (2024)].

[24] Lisa Stryjewski. 40 years of boxplots. 2010.

[25] Cristian L. Klunk, Marco A. Argenta, Alexandre Casadei-Ferreira, Evan P. Economo, and Marcio R. Pie. Mandibular morphology, task specialization and bite mechanics in pheidole ants (hymenoptera: Formicidae). *Journal of The Royal Society Interface*, 18(179):20210318, 2021.